日本磁気学会
ISSN 2432-0250
Journal of the Magnetics Society of Japan
Electronic Journal URL: https://www.jstage.jst.go.jp/browse/msjmag

Vol.47 No.1　2023

Journal

JOURNAL OF THE MAGNETICS SOCIETY OF JAPAN

Vol.47 No.1 2023

日本磁気学会

ISSN 2432-0250

HP: http://www.magnetics.jp/ e-mail: msj@bj.wakwak.com
Electronic Journal: http://www.jstage.jst.go.jp/browse/msjmag

TOEI

世界初！ 高温超電導型VSM

新製品

世界初*、高温超電導マグネットをVSMに採用することで測定速度 当社従来機1/20を実現。
0.5mm cube磁石のBr, HcJ高精度測定が可能となりました。

*2014年7月 東英工業調べ

測定結果例

高温超電導VSMによるNdFeB(sint.) 0.5mm cube BHカーブ

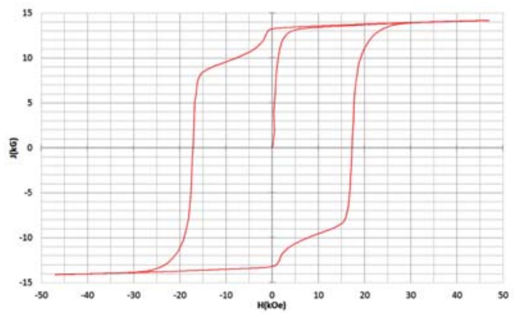

磁化測定レンジ：0.2emu
Br = 13.2kG　HcJ = 17.2kOe

高温超電導VSMによるNdFeB(sint.) 1mm cube BHカーブ

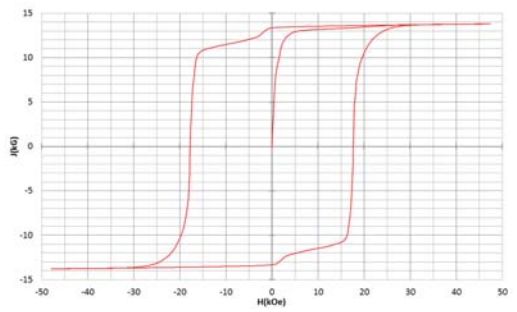

磁化測定レンジ：2emu
Br = 13.3kG　HcJ = 17.7kOe

高温超電導VSMによるNdFeB(sint.) 4mm cube BHカーブ

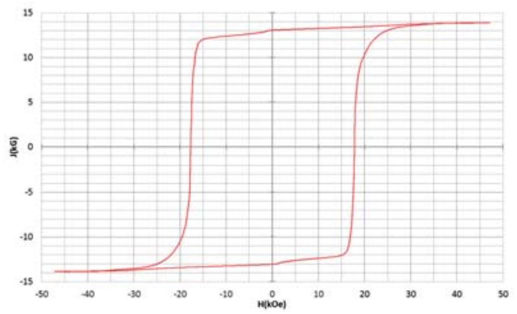

磁化測定レンジ：100emu
Br = 13.1kG　HcJ = 17.8kOe

高速測定を実現

高温超電導マグネット採用により、高速測定を実現しました。Hmax= 5Tesla, Full Loop 測定が2分で可能です。
（当社従来機：Full Loop測定 40分）

小試料のBr,HcJ 高精度測定

0.5mm cube 磁石のBr,HcJ 高精度測定ができ、表面改質領域を切り出しBr,HcJ の強度分布等、微小変化量の比較測定が可能です。
また、試料の加工劣化の比較測定が可能です。

試料温度可変測定

−50℃～+200℃温度可変UNIT（オプション）

磁界発生部の小型化

マグネットシステム部寸法：0.8m×0.3m×0.3m

TOEI 東英工業株式会社
http://www.toeikogyo.co.jp
〒194-0035 東京都町田市忠生1-8-13
TEL：042-791-1211 FAX：042-792-0490
E-mail：sales@toeikogyo.co.jp

Journal of the Magnetics Society of Japan

Vol. 47, No. 1

Electronic Journal URL: https://www.jstage.jst.go.jp/browse/msjmag

CONTENTS

INDEX

J. Magn. Soc. Jpn., **47**, 1-14 (2023)

<Paper>

Comparison of Shingled Heat-Assisted Magnetic Recording and Three-Dimensional Heat-Assisted Magnetic Recording

T. Kobayashi, Y. Nakatani*, and Y. Fujiwara
Graduate School of Engineering, Mie Univ., *1577 Kurimamachiya-cho, Tsu 514-8507, Japan*
*Graduate School of Informatics and Engineering, Univ. of Electro-Communications, *1-5-1 Chofugaoka, Chofu 182-8585, Japan*

In this work we examine grain arrangement and medium structure, temperature profile during writing, adjacent track interference, information stability during 10 years of archiving, information stability in a high Curie temperature (HC) layer during writing in a low Curie temperature (LC) layer, and writing sensitivity on 4 Tbpsi shingled heat-assisted magnetic recording (HAMR) with a bit aspect ratio of 1.5 and 2 Tbpsi/layer (total density of 4 Tbpsi) three-dimensional (3D) HAMR with bit aspect ratios of 1.0 and 2.0. A small bit aspect ratio is preferable in 3D HAMR. The grain aspect ratios for both HAMR and 3D HAMR may be too large when it comes to manufacturing the recording layer. The low Curie temperature of the LC layer may be disadvantageous with respect to the writing property. The readout field is small for both the LC and HC layers in 3D HAMR. The writing sensitivity for HAMR is worse than that for 3D HAMR because the statistical factor is affected by the readout grain number and erasure-after-write is affected by the grain column number. Although both HAMR and 3D HAMR have disadvantages, the poor writing sensitivity in HAMR is a serious problem.

Key words: 3D HAMR, temperature profile, ATI, 10 years of archiving, LC writing, writing sensitivity, bit aspect ratio

1. Introduction

Heat-assisted magnetic recording (HAMR) has potential as a next-generation magnetic recording method with a high recording capacity. HAMR is a recording technique in which the medium is heated to reduce coercivity during the writing period. Three-dimensional HAMR (3D HAMR) has been proposed[1] where the medium consists of a high mean Curie temperature $T_{\rm HC}$ (HC) layer with a grain height $h_{\rm HC}$, a low mean Curie temperature $T_{\rm LC}$ (LC) layer with a grain height $h_{\rm LC}$, and an isolation layer inserted between the two layers to suppress exchange coupling between them. With 3D HAMR, once data have been written in the HC layer (HC writing), other data can be written in the LC layer (LC writing) by employing lower temperature heating. Yamane *et al.* reported a dual structure, namely 3D HAMR on bit patterned media[2].

We have previously discussed the medium layer structure in 3D HAMR on granular media[3], and adjacent track interference in HAMR[4]. Our research has led us to believe that the upper LC / lower HC layer structure is preferable if the problem of heat resistance can be solved.

It is important to establish whether or not 3D HAMR has an advantage over conventional HAMR. In this paper, we compared 4 Tbpsi shingled HAMR with 2 Tbpsi/layer (total density of 4 Tbpsi) 3D LC / HC HAMR, since 3D HAMR must be combined with shingled magnetic recording because of the large adjacent track interference in the LC layer during HC writing.

We must comprehensively consider all the factors when comparing shingled HAMR and 3D HAMR. Therefore, we examine

1.1 grain arrangement and medium structure,
1.2 temperature profile during writing,
1.3 adjacent track interference,
1.4 information stability during 10 years of archiving,
1.5 information stability in the HC layer during LC writing, and
1.6 writing sensitivity

on 4 Tbpsi shingled HAMR ($3 \times 2 = 6$ grains/bit) in section 3.1, 2 Tbpsi/layer 3D HAMR ($3 \times 3 = 9$ grains/bit) in 3.2, and 2 Tbpsi/layer 3D HAMR ($4 \times 2 = 8$ grains/bit) in 3.3, where one bit has m grains in the cross-track direction and n grains in the down-track direction, *i.e.*, there are $m \times n$ grains/bit.

2. Calculation Method and Conditions

2.1 Magnetic properties

The temperature dependence of the medium magnetization $M_{\rm s}$ was calculated by employing mean field analysis[5], and that of the medium anisotropy constant $K_{\rm u}$ was assumed to be proportional to $M_{\rm s}^2$[6]. $M_{\rm s}(T_{\rm c}, T)$ is a function of the Curie temperature $T_{\rm c}$ and temperature T. $M_{\rm s}(T_{\rm c} = 770\ {\rm K}, T = 300\ {\rm K}) = 1000$ emu/cm^3 was assumed for FePt, which is a potential HAMR medium material thanks to its large $K_{\rm u}$ and relatively low $T_{\rm c}$. Based on this assumption, the $M_{\rm s}$ value can be calculated for all values of $T_{\rm c}$ and T.

We have introduced an HAMR medium parameter, namely, the medium anisotropy constant ratio $K_{\rm u}/K_{\rm bulk}$[7] in place of $K_{\rm u}$, since the $K_{\rm u}$ value at the storage temperature is a function of $T_{\rm c}$, which is strongly related to the writing property. $K_{\rm u}/K_{\rm bulk}$ is the intrinsic ratio of the medium $K_{\rm u}$ to bulk FePt $K_{\rm u}$, which is independent of $T_{\rm c}$, and is valid for any temperature from zero Kelvin

Corresponding author: T. Kobayashi (e-mail: kobayasi@phen.mie-u.ac.jp).

to the Curie temperature.

The $K_u(T_c, K_u/K_{bulk}, T)$ value is a function of T_c, K_u/K_{bulk}, and T. $K_u(T_c = 770\,\text{K}, K_u/K_{bulk} = 1, T = 300\,\text{K}) = 70$ Merg/cm^3 was assumed for bulk FePt. Using this assumption, the K_u value can be calculated for all values of T_c, K_u/K_{bulk}, and T. No intrinsic distribution of K_u was assumed. However, there was a fluctuation in K_u caused by T_c variation.

The T_c value can be adjusted by changing the Cu composition z for $(Fe_{0.5}Pt_{0.5})_{1-z}Cu_z$.

2.2 Temperature profile

The thermal gradient during the writing period can be adjusted by changing the medium structure for HAMR. For simplicity, the thermal gradients $\partial T/\partial y$ of 8, 10, and 12 K/nm in the cross-track direction and $\partial T/\partial x$ of 0 in the down-track direction were assumed to be constant when we examined adjacent track interference. The $\partial T/\partial x$ of 8, 10, and 12 K/nm and $\partial T/\partial y$ of 0 were assumed to be constant when we examined writing sensitivity.

On the other hand, for 3D HAMR, since there is a correlation between the thermal gradients in the upper and lower layers, we used a previously published temperature profile[8], in which a heat transfer simulation was carried out using Poynting for Optics software (Fujitsu Ltd.). The light spot diameter was about 9.0 nm (FWHM) in the down-track and cross-track directions. The linear velocity was 10 m/s. The ambient temperature T_{amb} is the maximum working temperature of the hard disk drive, and was assumed to be 330 K.

We also focused on the medium surface temperature T_{surf} at the track center during HC writing, and the layer temperature difference ΔT_{HL} between the HC and LC layers at the track edges during LC writing.

2.3 Information stability

We assumed the medium to be granular. One bit has m grains in the cross-track (row i) direction and n grains in the down-track (column j) direction, *i.e.*, there are $m \times n$ grains/bit.

The information stability was estimated using the grain error probability P[9],

$$P = 1 - \exp\left(-f_0 t \exp\left(-\frac{K_{ueff}V}{kT}\left(1+\frac{H_w}{H_{keff}}\right)^2\right)\right),\quad (1)$$
$$(|H_w| < H_{keff})$$

taking account of the shape anisotropy $M_s H_d/2$ using a self-demagnetizing field H_d, where f_0, t, K_{ueff}, V, k, T, and H_w are, respectively, the attempt frequency[10], time, effective anisotropy constant, grain volume, Boltzmann constant, grain temperature, and writing field. The f_0 value is a function of the Gilbert damping constant α[10]. The α value used here was 0.1 without temperature dependence, since the α value and its temperature dependence for FePt near the Curie temperature are not currently known. $K_{ueff} = K_u - M_s H_d/2$, $H_d = 8M_s \arctan(D^2/(h\sqrt{2D^2+h^2}))$, $V = D \times D \times h$ where D and h are the grain size and height, respectively. However, H_d does not affect the results, as reported in a previous paper[11], since $K_u \gg M_s H_d/2$. Therefore, the magnetostatic field from surrounding grains can also be ignored. It was assumed that there was no exchange coupling between grains.

To evaluate the grain error distribution, we calculated the expected value of the magnetization $E[M_s]$,

$$E[M_s] = (1-P)M_s + P(-M_s) = (1-2P)M_s. \quad (2)$$

Since there is a temperature distribution in the cross-track direction during LC writing, the $E[M_s]$ value was averaged over one row of grains as

$$E[M_{si}] = \frac{\sum_{j=1}^{n}(1-2P_{ij})M_{sij}(T_{cij},\ 330\,\text{K})}{n} \quad (3)$$

at a readout temperature of 330 K.

The bit error rate bER was also calculated by employing P. For example, for 4 grains/bit, the bit error rate ${}_4\text{bER}_1$ for 1 grain error is expressed as

$$\begin{aligned}{}_4\text{bER}_1 = &\ Er_1 P_1(1-P_2)(1-P_3)(1-P_4) + \cdots \\ &+ Er_4(1-P_1)(1-P_2)(1-P_3)P_4, \end{aligned}\quad (4)$$

the bit error rate ${}_4\text{bER}_2$ for 2 grain errors as

$$\begin{aligned}{}_4\text{bER}_2 = &\ Er_{12} P_1 P_2(1-P_3)(1-P_4) + \cdots \\ &+ Er_{34}(1-P_1)(1-P_2)P_3 P_4, \end{aligned}\quad (5)$$

the bit error rate ${}_4\text{bER}_3$ for 3 grain errors as

$$\begin{aligned}{}_4\text{bER}_3 = &\ Er_{123} P_1 P_2 P_3(1-P_4) + \cdots \\ &+ Er_{234}(1-P_1)P_2 P_3 P_4, \end{aligned}\quad (6)$$

and the bit error rate ${}_4\text{bER}_4$ for 4 grain errors as

$${}_4\text{bER}_4 = P_1 P_2 P_3 P_4, \quad (7)$$

where

$$Er_k = 1, \text{ if } \frac{\sum_{i,j} M_{sij}(T_{cij},\ 330\,\text{K})D_{ij}^2}{(m\times n)M_s(T_{cm},\ 330\,\text{K})D_m^2} \le E_{th}, \quad (8)$$

and

$$Er_k = 0, \text{ if } \frac{\sum_{i,j} M_{sij}(T_{cij},\ 330\,\text{K})D_{ij}^2}{(m\times n)M_s(T_{cm},\ 330\,\text{K})D_m^2} > E_{th}, \quad (9)$$

where T_{cm} and D_m are the mean Curie temperature and the mean grain size, respectively. Errors occur in some grains of a bit. We assumed that if the ratio of $\sum_{i,j} M_{sij}(T_{cij},\ 330\,\text{K})D_{ij}^2$ to $(m\times n)M_s(T_{cm},\ 330\,\text{K})D_m^2$ is greater than a calculation parameter named error threshold E_{th} as shown in Eq. (9), the bit will be error-free, namely $Er_k = 0$, where the numerator $\sum_{i,j} M_{sij}(T_{cij},\ 330\,\text{K})D_{ij}^2$ is the surface magnetic charge of the grains that are magnetized in the recording direction, and the denominator $(m\times n)M_s(T_{cm},\ 330\,\text{K})D_m^2$ is the total surface magnetic charge. M_{sij}, T_{cij}, and D_{ij} are, respectively, the magnetization, the Curie temperature, and the grain size of the ij-th grain. The total bit error rate ${}_4$bER is the summation of each bit error rate ${}_4\mathrm{bER}_k$ as follows

$$ {}_4\mathrm{bER} = \Sigma_k\, {}_4\mathrm{bER}_k. \quad (10)$$

Therefore, the bit error rate is a function of E_{th}. The calculation bit number was 10^7. The criterion determining whether or not information was stable was assumed to be a bER of 10^{-3}.

We defined the normalized readout field H_0 as a readout magnetic field normalized by that from the grains where all the grains possess T_{cm} and D_{m}, and all the grains are magnetized in the recording direction, which corresponds to the denominator in Eqs. (8) and (9). Therefore, H_0 can roughly be represented by E_{th} as

$$H_0 = 2E_{\mathrm{th}} - 1. \quad (11)$$

For example, assuming all the grains are homogeneous, E_{th} equals one when the magnetization directions of all the grains are parallel to the recording direction. The H_0 value becomes one. When the magnetization directions of half the grains are parallel, and those of the other half are antiparallel to the recording direction, E_{th} equals a half. The H_0 value becomes zero. The minimum normalized readout field, which must be readable without error after writing in the adjacent track (AT writing), after 10 years of archiving, and after LC writing, can be estimated with E_{th} to have a bER of 10^{-3}.

We also defined the information degradation rate R_0 during 10 years of archiving as

$$R_0 = \frac{\mathrm{bER(10.0\,yrs)} - \mathrm{bER(0.001\,yrs)}}{\mathrm{bER(0.001\,yrs)}}, \quad (12)$$

where 0.001 years corresponds to about 9 hours. For example, the R_0 values are 99, 9.0, and 0.11 when the bER(0.001 yrs) values are 10^{-5}, 10^{-4}, and 9×10^{-4}, respectively, since the bER(10.0 yrs) value is 10^{-3}. The R_0 value for no information degradation is less than about 0.1.

2.4 Field strength

The flying height was 4.0 nm, which is the distance between the magnetic head reader and the recording layer surface.

The magnetic field strength from the medium at the center of readout row m_{R} (see Fig. 1) grains and at the reader position was calculated using $m_{\mathrm{R}} \times 30$ grains with no grain size distribution and no T_{c} variation when calculating the field strength.

2.5 Writing sensitivity

We examined the writing field H_{w} dependence of the signal to noise ratio SNR by employing a micromagnetic calculation using the Landau-Lifshitz-Gilbert (LLG) equation where the magnetic properties used here change with temperature. The temperature dependence was calculated using mean field analysis. We believe that the use of the LLG equation that includes the temperature dependence of magnetic properties is a suitable replacement for the Landau-Lifshitz-Bloch (LLB) equation. We also examined the H_{w} dependence of the bER using our model calculation[12], with the aim of grasping the physical implications of the writing property in HAMR.

The α value used here was 0.1 without temperature dependence. The linear velocity v was 10 m/s. For simplicity, the thermal gradients $\partial T/\partial x$ and $\partial T/\partial y$ of 0 were assumed to be uniformly constant. The writing field was assumed to be spatially uniform, the direction to be perpendicular to the medium plane, the recording frequency to be $v/(2D_{\mathrm{B}})$, and the rise time to be zero, where D_{B} is the bit length. The demagnetizing field inside the grain was included, but the magnetostatic field from surrounding grains during writing was neglected.

In the LLG calculation, the output signal, media noise, and media SNR were calculated using a sensitivity function[13], which is the same as the cross-track width of the simulation region, a magnetoresistive read head with a 15 nm shield-shield spacing, and a 4.0 nm head-medium spacing for 2 Tbpsi and 6 grains/bit shingled HAMR with a D_{B} of 14.7 nm[4]. Since the SNR value is also affected by the resolution of the read head, we changed the shield-shield spacing to $(D_{\mathrm{B}}/14.7) \times 15$ nm for other calculations. The number of the grains for the down-track direction was fixed at 2304. Simulation was repeated 32 times for each condition with different grain size distribution patterns with same averaged size and deviation, and the averaged SNR value was obtained.

In the model calculation, the resolution of the read head corresponds to infinity. The calculation bit number was 10^6. The bER value in this paper is useful only for comparisons such as information stability and writing sensitivity between various media.

3. Calculation Results

3.1 4 Tbpsi shingled HAMR (3 × 2 = 6 grains/bit)

3.1.1 Grain arrangement and medium structure

There is a trade-off relationship between adjacent track interference (ATI) and writing sensitivity, since ATI means writing in the adjacent track[4]:

(1) Grain number per bit

Reducing the grain number per bit improves ATI, since the grain temperature can be reduced due to the larger grain pitch.

Reducing the grain number per bit worsens the writing sensitivity. The bER increases with decreasing grain number, since the probability of a simultaneous error in grains becomes statistically higher.

(2) Grain height (recording layer thickness)

Increasing the grain height h improves ATI, since the thermal stability factor $K_{\mathrm{ueff}}V/(kT)$ becomes larger due to the larger $V = D \times D \times h$ value.

Increasing the h value worsens the writing sensitivity for the same reason.

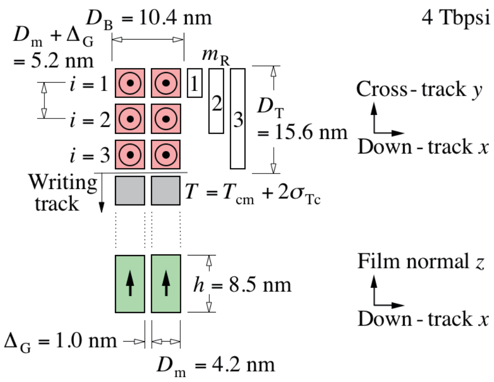

Fig. 1 Grain arrangement and medium structure in 4 Tbpsi shingled HAMR (3 × 2 = 6 grains/bit).

Table 1 Grain and bit sizes in 4 Tbpsi shingled HAMR (3 × 2 = 6 grains/bit).

	Shingled HAMR
Grain height h (nm)	8.5
Mean grain size D_m (nm)	4.2
Standard deviation σ_D / D_m (%) of D_m	15
Grain aspect ratio h / D_m	2.0
Grain volume V (nm^3)	149
Track width D_T (nm)	15.6
Bit length D_B (nm)	10.4
Bit aspect ratio D_T / D_B	1.5

(3) Grain aspect ratio

Furthermore, the simultaneous realization of a small D_m value, large grain aspect ratio h/D_m, and large anisotropy constant appears to make it too difficult to manufacture a recording layer.

The design of grain number per bit and grain height is affected by above factors (1), (2), and (3). We chose a grain arrangement of $m \times n$ = 3×2 = 6 grains/bit and an h value of 8.5 nm, taking account of factors (1) and (2) (see Figs. 3 and 6), respectively, as shown in Fig. 1. Factor (3) is currently being experimentally investigated by many researchers[14,15].

The writing temperature of the grains at the edge of the writing track was assumed to be $T_{cm} + 2\sigma_{Tc}$, taking account of the standard deviation σ_{Tc} of the mean Curie temperature T_{cm}. Based on this assumption, almost all grains in the writing track are heated to above their Curie temperatures during the writing period.

The bER value is a function of the readout track width after AT writing. We therefore calculated the bER and the H_0 values for readout rows m_R of 1 (i = 1), 2 (i = 1 and 2), and 3 (i = 1, 2, and 3).

The grain and bit sizes are summarized in Table 1. The D_m value was determined by

Table 2 Temperature profile in 4 Tbpsi shingled HAMR (3 × 2 = 6 grains/bit).

	Shingled HAMR
Anisotropy constant ratio K_u / K_{bulk}	0.8
Mean Curie temperature T_{cm} (K)	750
Standard deviation σ_{Tc} / T_{cm} (%) of T_{cm}	2
(Temperature profile)	
Thermal gradient $\partial T / \partial x$ (K / nm)	8, 10, 12
Thermal gradient $\partial T / \partial y$ (K / nm)	8, 10, 12

$$D_m = \sqrt{\frac{S}{m \times n}} - \Delta_G, \quad (13)$$

where S is the bit area for 4 Tbpsi. We assumed the intergrain spacing Δ_G to be 1.0 nm regardless of the recording density and the grain number per bit. The grain size distribution was log-normal with a standard deviation σ_D/D_m of 15 % for D_m. The bit aspect ratio was $D_T/D_B = m/n$ where $D_T = m(D_m + \Delta_G)$, $D_B = n(D_m + \Delta_G)$, and $D_m + \Delta_G$ are the track width, bit length, and grain pitch, respectively.

The large h/D_m value of 2.0 may make it too difficult to manufacture the recording layer[15].

3.1.2 Temperature profile

We used a K_u/K_{bulk} value of 0.8 as shown in Table 2. When the T_c value is low, the anisotropy field obtained by the experiment does not decrease steeply toward T_c compared to that predicted by the theory[16]. Since this may be disadvantageous in terms of jitter to the writing property, a T_{cm} value of 750 K was used. The T_c distribution was normal with a standard deviation σ_{Tc}/T_{cm} of 2 % for T_{cm}. The T_c variation means that the writing time is advanced or delayed. For example, the advanced and delayed times correspond to $\sigma_{Tc}/(v \cdot \partial T/\partial x)$ for grains with $T_c = T_{cm} + \sigma_{Tc}$ and $T_c = T_{cm} - \sigma_{Tc}$, respectively[17]. Therefore, the σ_{Tc} is equivalent to the standard deviation σ_x of the grain position as $\sigma_x = \sigma_{Tc}/(\partial T/\partial x)$. For example, σ_x/D_m is about 30 % when the σ_{Tc}/T_{cm} and $\partial T/\partial x$ values are 2 % and 12 K/nm, respectively. Therefore, the value of 2 % includes σ_{Tc}/T_{cm} and σ_x/D_m.

3.1.3 Adjacent track interference

Figure 2 shows the minimum normalized readout field H_0 for various numbers of readout rows m_R (see Fig. 1) after AT writing. Time t and the writing field H_w were assumed to be 1 ns and −10 kOe, respectively.

There is no H_0 greater than 0 that satisfies a bER of 10^{-3} for m_R of 3. Therefore, the 3rd row (i = 3) grains is used as a guard band. The $\partial T/\partial y$ value of more than about 12 K/nm is necessary to improve ATI. The temperature at the 1st row (i = 1) is obviously lower than that at the 2nd row (i = 2). However, when $\partial T/\partial y$ equals 12 K/nm, Fig. 2 shows the H_0 value for an m_R of

2 (i = 1 and 2) to be greater than that for an m_R of 1 (i = 1) for a statistical reason.

For an m_R of 2 ($m_R \times n$ = 2 × 2 = 4 grains), Fig. 3 shows the bER value as a function of E_{th} before and after AT writing for various grain heights h. The second horizontal axis is the H_0 value estimated using Eq. (11).

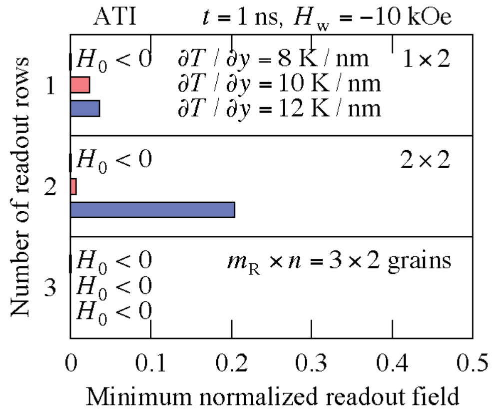

Fig. 2 Minimum normalized readout field H_0 for various numbers of readout rows m_R (see Fig. 1) after adjacent track (AT) writing in 4 Tbpsi shingled HAMR (3 × 2 = 6 grains/bit).

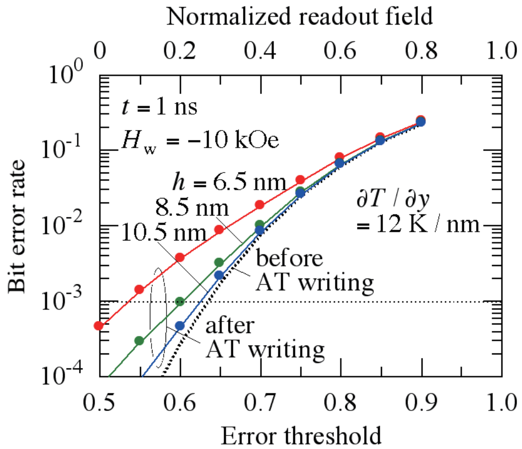

Fig. 3 Bit error rate as a function of error threshold E_{th} and normalized readout field H_0 before and after AT writing for various grain heights h in 4 Tbpsi shingled HAMR (2 × 2 = 4 grains).

Table 3 Adjacent track interference in 4 Tbpsi shingled HAMR (3 × 2 = 6 grains/bit).

	Shingled HAMR
(Adjacent track interference)	
Thermal gradient $\partial T / \partial y$ (K / nm)	12
Readout grain number $m_R \times n$	2 × 2
Readout track width D_{RT} (nm)	9.4
Minimum normalized readout field H_0	0.20
Peak z component H_{zpeak} (Oe)	1197
$D_{RT} \times H_0 \times H_{zpeak}$ (knmOe)	2.3

The bER value increases as the h value decreases, since the $K_{ueff}V/(kT)$ value becomes smaller due to the smaller $V = D \times D \times h$ value[4]. There is almost no increase in the bER after AT writing for an h of 10.5 nm. On the other hand, a considerable increase can be seen in the bER for an h of 6.5 nm.

The ATI results are summarized in Table 3 for a $\partial T/\partial y$ of 12 K/nm. The resultant readout grain number $m_R \times n$ and readout track width D_{RT} are 2 × 2 and 9.4 nm, respectively. The H_0 value, that must be readable without error after AT writing, and the peak z component H_{zpeak} of the readout field for an m_R of 2 are 0.20 and 1197 Oe, respectively. We roughly evaluated the readout property using the $D_{RT} \times H_0 \times H_{zpeak}$ product. The $D_{RT} \times H_0 \times H_{zpeak}$ product is 2.3 knmOe.

3.1.4 10 years of archiving

We examined the information stability for 10 years of archiving with no H_w. The storage temperature was 350 K. We took a certain temperature margin into account. Figure 4 (a) shows that since 2 grains in 6 grains/bit are used as a guard band, the bER value after 10 years of

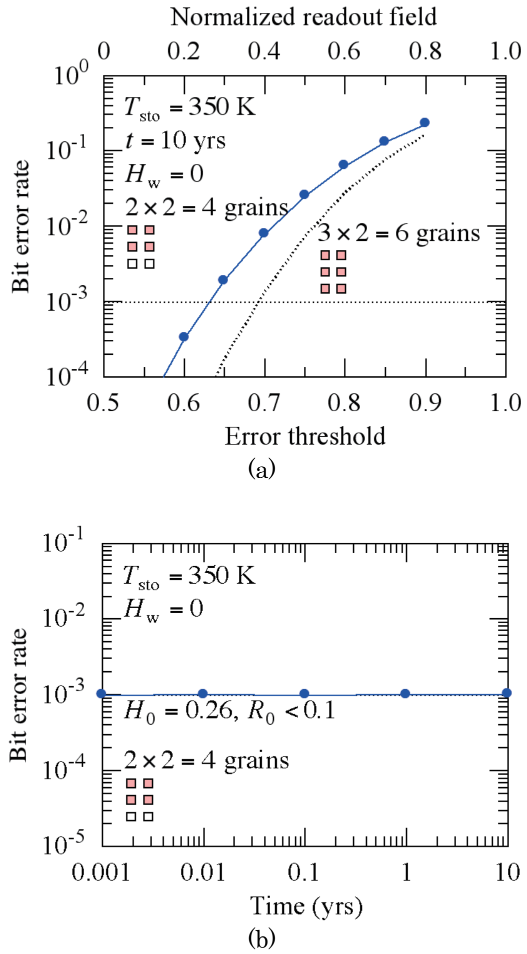

Fig. 4 (a) Bit error rate as a function of error threshold E_{th} and normalized readout field H_0 after 10 years of archiving and (b) time dependence of bit error rate during 10 years of archiving in 4 Tbpsi shingled HAMR (2 × 2 = 4 grains).

Table 4 10 years of archiving in 4 Tbpsi shingled HAMR ($3 \times 2 = 6$ grains/bit).

	Shingled HAMR
(10 years of archiving)	
$K_{ueff}V/(kT)$ (T = 350 K)	152
Minimum normalized readout field H_0	0.26
$D_{RT} \times H_0 \times H_{zpeak}$ (knmOe)	3.0
Information degradation rate R_0	<0.1

archiving for $m_R \times n = 2 \times 2 = 4$ grains is higher than that for $m \times n = 3 \times 2 = 6$ grains for a statistical reason. Table 4 shows that the H_0 value for m_R of 2 that must be readable without error after 10 years of archiving is 0.26, and the $D_{RT} \times H_0 \times H_{zpeak}$ product is 3.0 knmOe. Since the $D_{RT} \times H_0 \times H_{zpeak}$ product is 2.3 knmOe for ATI as shown in Table 3, the limiting factor is ATI.

Since the $K_{ueff}V/(kT)$ value of 152 is sufficiently large, the R_0 value is less than 0.1 as shown in Table 4. Therefore, no information degradation can be seen during 10 years as shown in Fig. 4 (b).

3.1.5 Writing sensitivity

For an m_R of 2 ($m_R \times n = 2 \times 2 = 4$ grains), Fig. 5 shows the writing field H_w dependence of (a) SNR calculated using the LLG equation and (b) bER using our model for various $\partial T/\partial x$ values. Our model calculation can almost entirely explain the results of the LLG simulation. Therefore, the physical implications of the writing property can be grasped by employing our model.

A relatively large H_w is needed to increase the SNR or to reduce the bER, which means that the writing sensitivity is worse. Furthermore, the influence of erasure-after-write (EAW) is strongly evident in the relatively large H_w region. EAW consists of grain magnetization reversal in the opposite direction to the recording direction. This is caused by the change in the writing field direction at the end of the writing time. EAW thus occurs after writing. A $\partial T/\partial x$ value of more than about 12 K/nm is needed to suppress EAW[17].

The H_w dependence of the bER for various grain heights h is shown in Fig. 6. The bER value increases as the h value increases, which means that the writing sensitivity worsens as the h value increases, since the $K_{ueff}V/(kT)$ value becomes larger due to the larger $V = D \times D \times h$ value[4]. As regards h, there is a trade-off relationship between ATI as shown in Fig. 3 and writing sensitivity as shown in Fig. 6, since ATI means writing in the adjacent track.

Figure 7 shows the H_w dependence of the bER for 1 bit ("010" data using $2 \times 2 = 4$ grains) and 2 bits of data ("0110" data using $2 \times 4 = 8$ grains). The bER value for

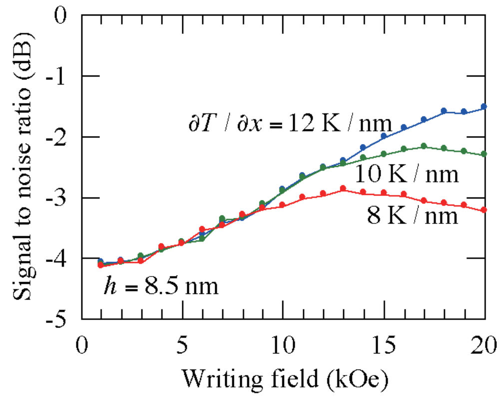

(a)

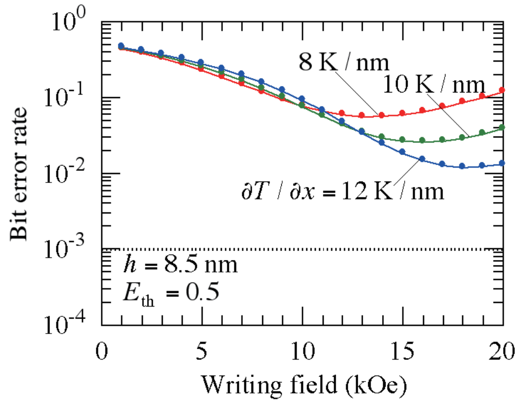

(b)

Fig. 5 Writing field H_w dependence of (a) signal to noise ratio and (b) bit error rate for various thermal gradients $\partial T/\partial x$ in 4 Tbpsi shingled HAMR ($2 \times 2 = 4$ grains).

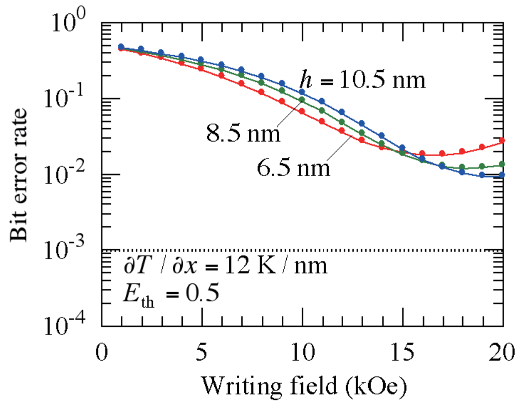

Fig. 6 Writing field H_w dependence of bit error rate for various grain heights h in 4 Tbpsi shingled HAMR ($2 \times 2 = 4$ grains).

2 bits of data is considerably smaller than that for 1 bit of data. Since the readout resolution corresponds to infinity, the bER value is not affected by the resolution of the read head. The reasons for the difference in bER are the statistical factor affected by the grain number and EAW affected by the grain column number[17].

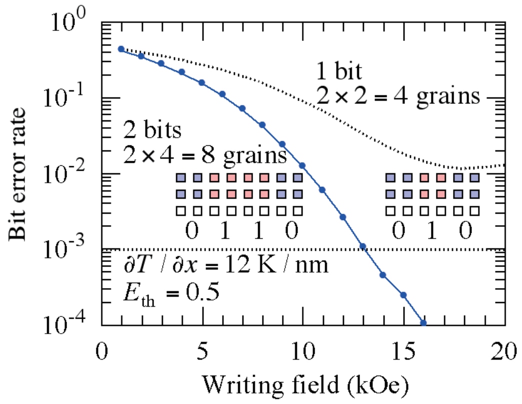

Fig. 7 Writing field H_w dependence of bit error rate for 1 bit ("010" data using 2 × 2 = 4 grains) and 2 bits of data ("0110" data using 2 × 4 = 8 grains) in 4 Tbpsi shingled HAMR.

3.2 2 Tbpsi/layer 3D HAMR (3 × 3 = 9 grains/bit)

3.2.1 Grain arrangement and medium structure

Figure 8 shows the grain arrangement and medium structure in 2 Tbpsi/layer 3D HAMR (3 × 3 = 9 grains/bit). The grain heights were revised for the LC and HC layers[3], taking account of ATI and 10 years of archiving. The grain and bit sizes are summarized in Table 5. The $(h_{LC} + h_{HC})/D_m$ value of 2.1 is relatively large as well as the h/D_m value of 2.0 for HAMR as shown in Table 1.

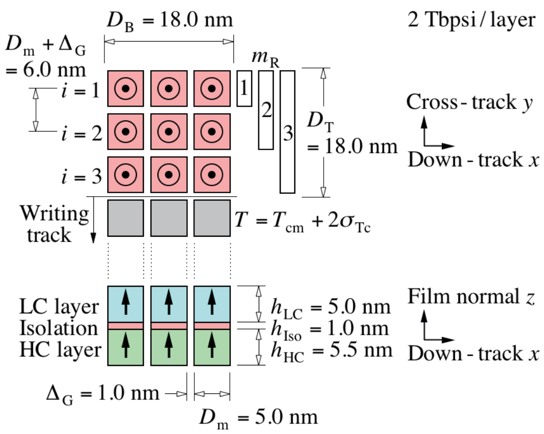

Fig. 8 Grain arrangement and medium structure in 2 Tbpsi/layer 3D HAMR (3 × 3 = 9 grains/bit).

Table 5 Grain and bit sizes in 2 Tbpsi/layer 3D HAMR (3 × 3 = 9 grains/bit).

	LC / HC	
	LC	HC
Grain height h_{LC}, h_{HC} (nm)	5.0	5.5
Mean grain size D_m (nm)	5.0	
Standard deviation σ_D / D_m (%) of D_m	15	
Grain aspect ratio $(h_{LC} + h_{HC}) / D_m$	2.1	
Grain volume V (nm^3)	124	137
Track width D_T (nm)	18.0	
Bit length D_B (nm)	18.0	
Bit aspect ratio D_T / D_B	1.0	

3.2.2 Temperature profile

Figures 9 (a) and (b) show the temperature profiles calculated by employing a heat transfer simulation for the cross-track direction during HC and LC writing, respectively.

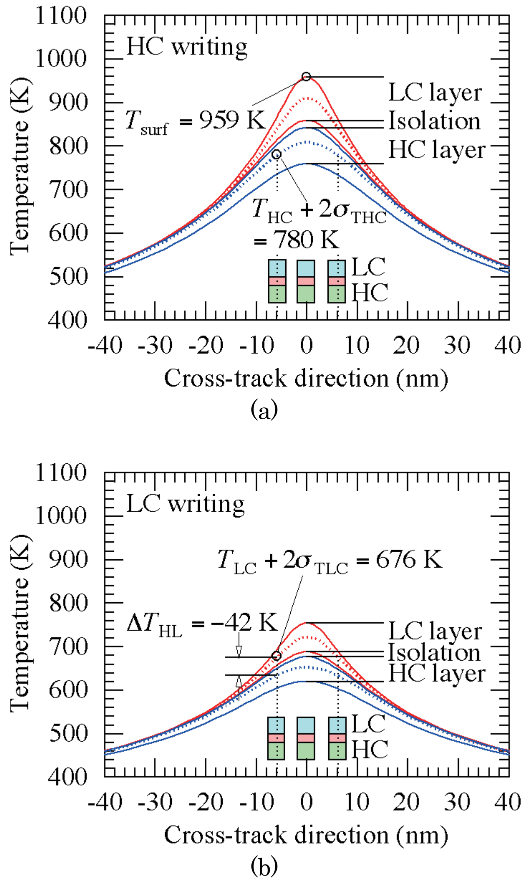

Fig. 9 Temperature profile for cross-track direction during (a) HC and (b) LC writing in 2 Tbpsi/layer 3D HAMR (3 × 3 = 9 grains/bit).

Table 6 Temperature profile in 2 Tbpsi/layer 3D HAMR (3 × 3 = 9 grains/bit).

	LC / HC	
	LC	HC
Anisotropy constant ratio K_u / K_{bulk}	0.8	
Mean Curie temperature T_{cm} (K)	650	750
Standard deviation σ_{Tc} / T_{cm} (%) of T_{cm}	2	
(Temperature profile)		
Surface temperature T_{surf} (K)		959
Layer temperature difference ΔT_{HL} (K)	−42	
Thermal gradient $\partial T / \partial x$ (K / nm)	11.9	8.8
Thermal gradient $\partial T / \partial y$ (K / nm)	11.8	8.8

The solid lines indicate the temperatures at the layer boundaries, and the dotted lines indicate those at the layer centers. The temperature profile results are summarized in Table 6.

(a) HC writing

The temperature at the track edge and the HC layer center is $T_{HC} + 2\sigma_{THC}$ = 780 K at which $\partial T_H/\partial y$ is 8.8 K/nm. The T_{surf} value of 959 K is relatively high, since HC is the lower layer. This is disadvantageous in terms of the heat resistance of the writing head and/or the surface lubricant.

(b) LC writing

The temperature at the track edge and the LC layer center is $T_{LC} + 2\sigma_{TLC}$ = 676 K at which $\partial T_L/\partial y$ is 11.8 K/nm. The negative ΔT_{HL} value of −42 K means that the temperature in the HC layer is lower than that in the LC layer, and this is advantageous in terms of information stability in the HC layer during LC writing.

We have previously reported the thermal gradient in 3D HAMR[8]:

(1) The thermal gradient for the upper layer is intrinsically larger than that for the lower layer due to a heat flow in the in-plane direction in the deep part of the layer.

(2) The thermal gradient for the HC layer is intrinsically larger than that for the LC layer due to their respective Curie temperatures.

Although $T_{HC} > T_{LC}$, the $\partial T_H/\partial y$ value of 8.8 K/nm is smaller than the $\partial T_L/\partial y$ value of 11.8 K/nm as shown in Table 6, since HC is the lower layer.

The low T_{LC} value of 650 K may be disadvantageous as regards the HAMR writing property, since the temperature dependence of the anisotropy field is somewhat smaller than that predicted by the theory[16].

3.2.3 Adjacent track interference

The H_0 value for various m_R values after AT writing is shown in Fig. 10. There is no H_0 greater than 0 that satisfies a bER of 10^{-3} for an m_R of 3 as well as the result for HAMR as shown in Fig. 2. Therefore, the 3rd row (i = 3) grains is used as a guard band.

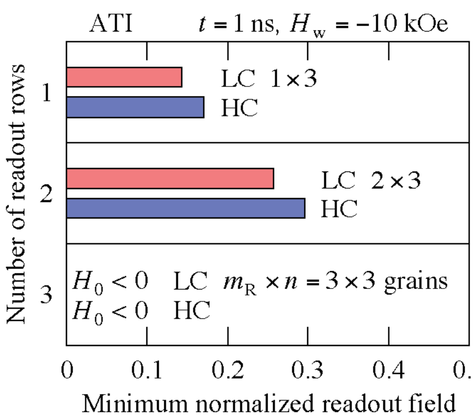

Fig. 10 Minimum normalized readout field H_0 for various numbers of readout rows m_R after AT writing in 2 Tbpsi/layer 3D HAMR (3 × 3 = 9 grains/bit).

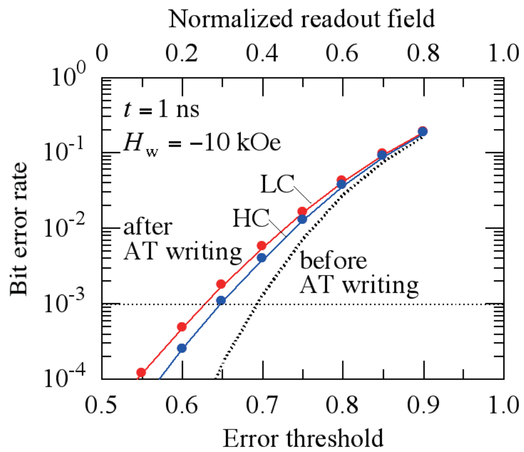

Fig. 11 Bit error rate as a function of error threshold E_{th} and normalized readout field H_0 before and after AT writing in 2 Tbpsi/layer 3D HAMR (2 × 3 = 6 grains).

Table 7 Adjacent track interference in 2 Tbpsi/layer 3D HAMR (3 × 3 = 9 grains/bit).

	LC / HC	
	LC	HC
(Adjacent track interference)		
Readout grain number $m_R \times n$	2 × 3	2 × 3
Readout track width D_{RT} (nm)	11.0	11.0
Minimum normalized readout field H_0	0.26	0.30
Peak z component H_{zpeak} (Oe)	1142	401
$D_{RT} \times H_0 \times H_{zpeak}$ (knmOe)	3.2	1.3

For an m_R of 2 ($m_R \times n$ = 2 × 3 = 6 grains), the bER value as a function of E_{th} before and after AT writing for the LC and HC layers is shown in Fig. 11. The bER value for 3D HAMR is smaller than that for HAMR as shown in Fig. 3 for a statistical reason affected by the grain number.

The ATI results are summarized in Table 7. The $m_R \times n$ and D_{RT} values are 2 × 3 and 11.0 nm, respectively. For the HC layer, although the H_0 value of 0.30 is relatively large, the H_{zpeak} value of 401 Oe is small due to the lower layer. The $D_{RT} \times H_0 \times H_{zpeak}$ product of 1.3 knmOe is small when compared with that of 2.3 knmOe for HAMR as shown in Table 3.

3.2.4 10 years of archiving

For an m_R of 2 ($m_R \times n$ = 2 × 3 = 6 grains), the bER value as a function of E_{th} after 10 years of archiving for the LC and HC layers is shown in Fig. 12 (a). The bER value for the LC layer is larger than that for the HC layer, since the h_{LC} and/or T_{LC} values are small. Table 8 shows that the H_0 value of 0.13 for the LC layer is small, and therefore, the $D_{RT} \times H_0 \times H_{zpeak}$ product of 1.6 knmOe is also small. Since the $D_{RT} \times H_0 \times H_{zpeak}$ product is 3.2 knmOe for ATI as shown in Table 7, the limiting factor for the LC layer is 10 years of archiving.

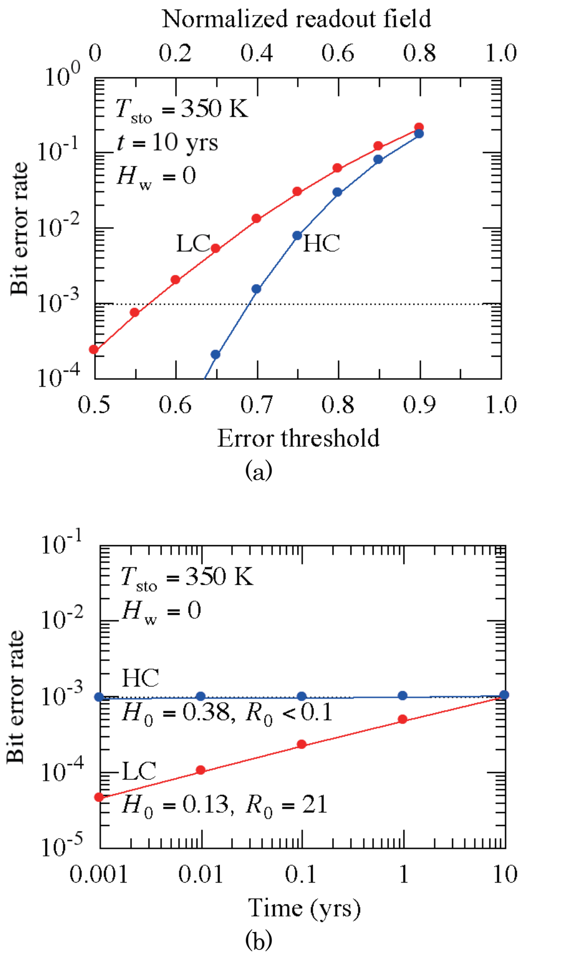

Fig. 12 (a) Bit error rate as a function of error threshold E_{th} and normalized readout field H_0 after 10 years of archiving and (b) time dependence of bit error rate during 10 years of archiving in 2 Tbpsi/layer 3D HAMR (2 × 3 = 6 grains).

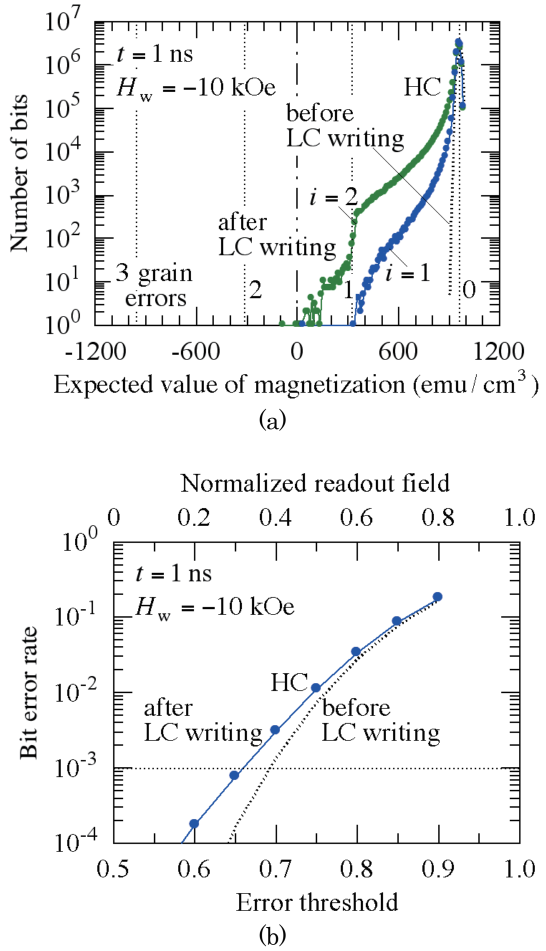

Fig. 13 (a) Number of bits plotted against expected value of magnetization $E[M_{si}]$ and (b) bit error rate for the HC layer as a function of error threshold E_{th} and normalized readout field H_0 before and after LC writing in 2 Tbpsi/layer 3D HAMR (2 × 3 = 6 grains).

Table 8 10 years of archiving in 2 Tbpsi/layer 3D HAMR (3 × 3 = 9 grains/bit).

	LC / HC	
	LC	HC
(10 years of archiving)		
$K_{ueff}V/(kT)$ (T = 350 K)	87	137
Minimum normalized readout field H_0	0.13	0.38
$D_{RT} \times H_0 \times H_{zpeak}$ (knmOe)	1.6	1.7
Information degradation rate R_0	21	< 0.1

Since the $K_{ueff}V/(kT)$ value of 87 for the LC layer is rather small, the R_0 value is 21 as shown in Table 8. Therefore, some information degradation can be seen during the 10 years as shown in Fig. 12 (b).

3.2.5 LC writing

For an m_R of 2 ($m_R \times n$ = 2 × 3 = 6 grains), Fig. 13 (a) shows the number of bits plotted against the expected value of magnetization $E[M_{si}]$ averaged over one-row grains for the HC layer before and after LC writing.

Table 9 LC writing in 2 Tbpsi/layer 3D HAMR (3 × 3 = 9 grains/bit).

	LC / HC	
	LC	HC
(LC writing)		
Minimum normalized readout field H_0		0.32
$D_{RT} \times H_0 \times H_{zpeak}$ (knmOe)		1.4

Time t and the writing field H_w were assumed to be 1 ns and −10 kOe, respectively. It also shows the grain error distribution. The negative $E[M_{si}]$ represents more than half of 3 grain errors, since the number of one-row grains n is three. The peaks in the figure represent the grain error for the grains with the mean Curie temperature. The grain error for the 2nd (i = 2) row is larger than that for the 1st (i = 1) row, since the temperature for the 2nd (i = 2) row is higher. There is no significant information degradation even in the 2nd (i = 2) row grains.

The bER value as a function of E_{th} for the HC layer

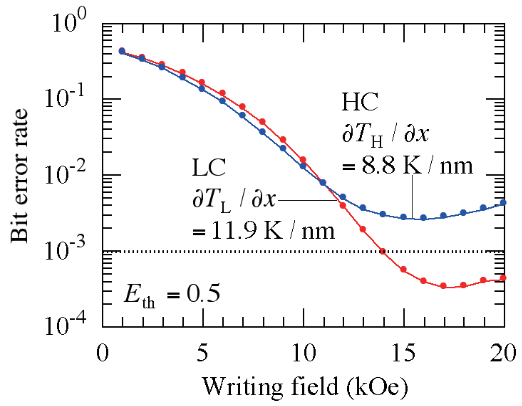

Fig. 14 Writing field H_w dependence of bit error rate in 2 Tbpsi/layer 3D HAMR ($2 \times 3 = 6$ grains).

before and after LC writing is shown in Fig. 13 (b). There is little information degradation for the HC layer during LC writing.

The H_0 values of 0.30, 0.38, and 0.32 for the HC layer are large for ATI, 10 years of archiving, and LC writing as shown in Tables 7, 8, and 9, respectively. However, the $D_{RT} \times H_0 \times H_{zpeak}$ products of 1.3, 1.7, and 1.4 knmOe for the HC layer are small as also shown in Tables 7, 8, and 9, respectively, since the H_{zpeak} value of 401 Oe is small as shown in Table 7 due to the lower HC layer. The limiting factor for the HC layer is thus the H_{zpeak} value.

3.2.6 Writing sensitivity

The bER value for 3D HAMR as shown in Fig. 14 is considerably smaller than that for HAMR as shown in Fig. 5. This means that the writing sensitivity for 3D HAMR is better than that for HAMR. Since the V values are 149, 124, and 137 nm³ for HAMR, the LC, and HC layers as shown in Tables 1 and 5, respectively, the reasons for the difference in bER are the statistical factor affected by the grain numbers $m_R \times n$ of 4 and 6, and EAW affected by the grain column numbers n of 2 and 3 for HAMR and 3D HAMR, respectively. EAW, which appeared in the relatively large H_w region, is rather large for the HC layer, since the $\partial T_H/\partial x$ value is rather small.

3.3 2 Tbpsi/layer 3D HAMR ($4 \times 2 = 8$ grains/bit)

3.3.1 Grain arrangement and medium structure

Before comparing HAMR and 3D HAMR, we examined the bit aspect ratio on 3D HAMR.

Figure 15 shows the grain arrangement and medium structure in 2 Tbpsi/layer 3D HAMR ($4 \times 2 = 8$ grains/bit). The grain and bit sizes are summarized in Table 10.

3.3.2 Temperature profile

Figures 16 (a) and (b) show the temperature profiles for the cross-track direction during HC and LC writing, respectively. The temperature profile results are summarized in Table 11.

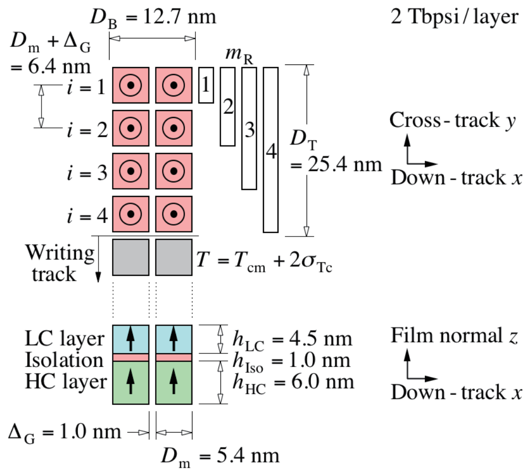

Fig. 15 Grain arrangement and medium structure in 2 Tbpsi/layer 3D HAMR ($4 \times 2 = 8$ grains/bit).

Table 10 Grain and bit sizes in 2 Tbpsi/layer 3D HAMR ($4 \times 2 = 8$ grains/bit).

	LC / HC	
	LC	HC
Grain height h_{LC}, h_{HC} (nm)	4.5	6.0
Mean grain size D_m (nm)	5.4	
Standard deviation σ_D / D_m (%) of D_m	15	
Grain aspect ratio $(h_{LC} + h_{HC}) / D_m$	2.0	
Grain volume V (nm^3)	129	172
Track width D_T (nm)	25.4	
Bit length D_B (nm)	12.7	
Bit aspect ratio D_T / D_B	2.0	

(a) HC writing

The T_{surf} value of 1009 K in Fig. 16 (a) for 3D HAMR with $4 \times 2 = 8$ grains/bit is higher than that of 959 K in Fig. 9 (a) for 3D HAMR with $3 \times 3 = 9$ grains/bit. Since the temperatures $T_{HC} + 2\sigma_{THC} = 780$ K at the track edge are the same, the T_{surf} value increases as the D_T value increases as shown in Figs. 9 (a) and 16 (a). Increasing the bit aspect ratio is disadvantageous in terms of the heat resistance of the writing head and/or the surface lubricant.

(b) LC writing

The $|\Delta T_{HL}|$ value of 29 K in Fig. 16 (b) is smaller than that of 42 K in Fig. 9 (b). The temperature difference between the LC and HC layers becomes smaller as the cross-track position is far from the track center as shown in Fig. 16 (b). Therefore, the $|\Delta T_{HL}|$ value decreases as the D_T value increases as shown in Figs. 9 (b) and 16 (b). Increasing the bit aspect ratio is also disadvantageous in terms of the information stability in the HC layer during LC writing.

Furthermore, since the $|\Delta T_{HL}|$ value is small, the difference between the $\partial T/\partial y$ values of the LC and HC layers is relatively small.

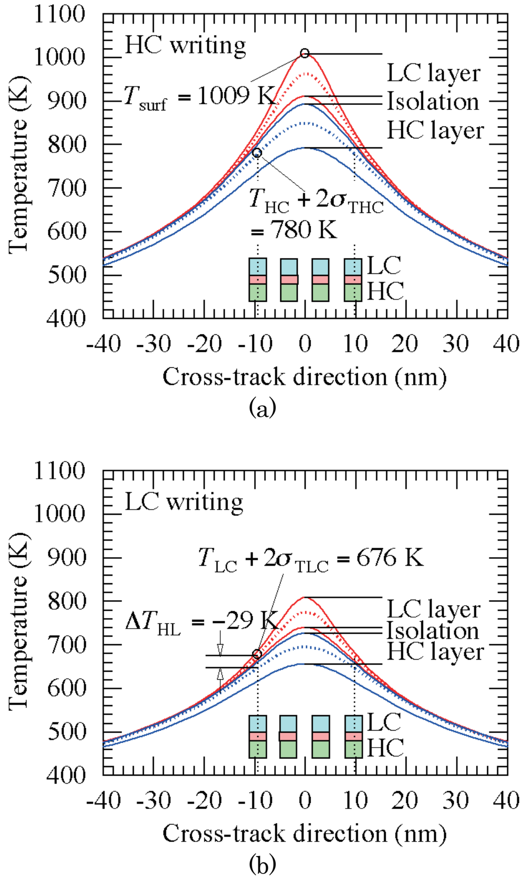

Fig. 16 Temperature profile for cross-track direction during (a) HC and (b) LC writing in 2 Tbpsi/layer 3D HAMR (4 × 2 = 8 grains/bit).

Table 11 Temperature profile in 2 Tbpsi/layer 3D HAMR (4 × 2 = 8 grains/bit).

	LC / HC	
	LC	HC
Anisotropy constant ratio K_u / K_{bulk}	0.8	
Mean Curie temperature T_{cm} (K)	650	750
Standard deviation σ_{Tc} / T_{cm} (%) of T_{cm}	2	
(Temperature profile)		
Surface temperature T_{surf} (K)		1009
Layer temperature difference ΔT_{HL} (K)	−29	
Thermal gradient $\partial T / \partial x$ (K / nm)	12.2	11.3
Thermal gradient $\partial T / \partial y$ (K / nm)	12.2	11.4

3.3.3 Adjacent track interference

The H_0 values for various m_R values after AT writing are shown in Fig. 17. A comparison with the result in Fig. 10 shows that ATI can be improved by increasing the bit aspect ratio. However, the 4th row (i = 4) grains is still used as a guard band. The readout grain numbers $m_R \times n$ = 2 × 3 = 6 grains and 3 × 2 = 6 grains are still the same for 3D HAMR with 3 × 3 = 9 grains/bit and 4 × 2 = 8 grains/bit, respectively.

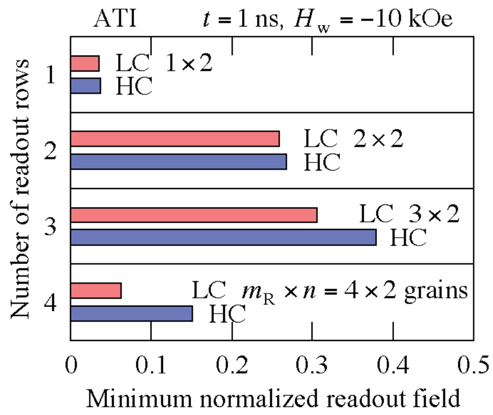

Fig. 17 Minimum normalized readout field H_0 for various numbers of readout rows m_R after AT writing in 2 Tbpsi/layer 3D HAMR (4 × 2 = 8 grains/bit).

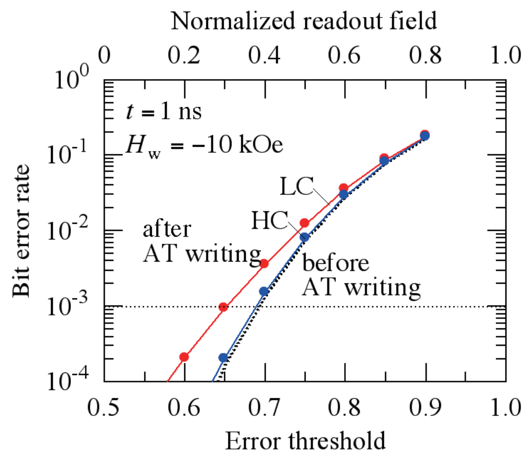

Fig. 18 Bit error rate as a function of error threshold E_{th} and normalized readout field H_0 before and after AT writing in 2 Tbpsi/layer 3D HAMR (3 × 2 = 6 grains).

Table 12 Adjacent track interference in 2 Tbpsi/layer 3D HAMR (4 × 2 = 8 grains/bit).

	LC / HC	
	LC	HC
(Adjacent track interference)		
Readout grain number $m_R \times n$	3 × 2	3 × 2
Readout track width D_{RT} (nm)	18.1	18.1
Minimum normalized readout field H_0	0.31	0.38
Peak z component H_{zpeak} (Oe)	1100	377
$D_{RT} \times H_0 \times H_{zpeak}$ (knmOe)	6.1	2.6

For an m_R of 3 ($m_R \times n$ = 3 × 2 = 6 grains), the bER value as a function of E_{th} before and after AT writing for the LC and HC layers is shown in Fig. 18. There is almost no information degradation of the HC layer during AT writing.

The ATI results are summarized in Table 12. The $m_R \times n$ and D_{RT} values are 3 × 2 and 18.1 nm, respectively. For the HC layer, although the H_{zpeak} value of 377 Oe is small, the $D_{RT} \times H_0 \times H_{zpeak}$ product of 2.6 knmOe is large when compared with that of 2.3 knmOe for HAMR as shown in Table 3, since the D_{RT} value of 18.1 nm is large.

3.3.4 10 years of archiving

When 3D HAMR with $3 \times 3 = 9$ grains/bit and with $4 \times 2 = 8$ grains/bit are compared, the results for 10 years of archiving, as shown in Figs. 12 and 19, are almost the same, since the V values of 124 and 129 nm³ are almost the same for the LC layer as shown in Tables 5 and 10, and the $K_{ueff}V/(kT)$ values of 137 and 172 are sufficiently large for the HC layer as shown in Tables 8 and 13, respectively. Although the H_0 value of 0.17 for the LC layer is small, the $D_{RT} \times H_0 \times H_{zpeak}$ product of 3.4 knmOe is large as shown in Table 13, because the D_{RT} value is large. Since the $D_{RT} \times H_0 \times H_{zpeak}$ product is 6.1 knmOe for ATI as shown in Table 12, the limiting factor for the LC layer is 10 years of archiving. The $D_{RT} \times H_0 \times H_{zpeak}$ product of 3.4 knmOe for the LC layer is larger than that of 2.3 knmOe for HAMR as shown in Table 3.

For the HC layer, the $D_{RT} \times H_0 \times H_{zpeak}$ products for ATI and 10 years of archiving are almost the same as shown in Tables 12 and 13. The $D_{RT} \times H_0 \times H_{zpeak}$ product of 2.6 knmOe for the HC layer is larger than that of 2.3 knmOe for HAMR as shown in Table 3.

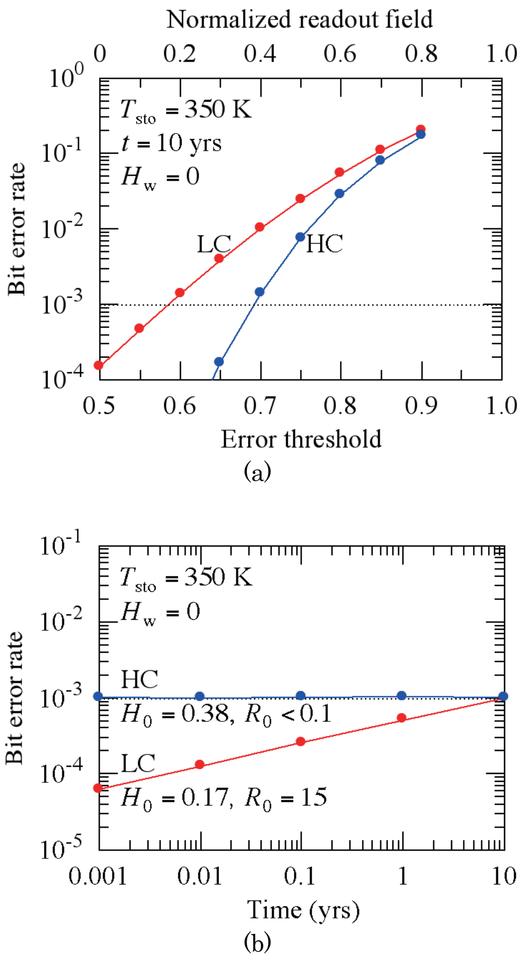

Fig. 19 (a) Bit error rate as a function of error threshold E_{th} and normalized readout field H_0 after 10 years of archiving and (b) time dependence of bit error rate during 10 years of archiving in 2 Tbpsi/layer 3D HAMR ($3 \times 2 = 6$ grains).

Table 13 10 years of archiving in 2 Tbpsi/layer 3D HAMR ($4 \times 2 = 8$ grains/bit).

	LC / HC	
	LC	HC
(10 years of archiving)		
$K_{ueff}V/(kT)$ (T = 350 K)	89	172
Minimum normalized readout field H_0	0.17	0.38
$D_{RT} \times H_0 \times H_{zpeak}$ (knmOe)	3.4	2.6
Information degradation rate R_0	15	<0.1

3.3.5 LC writing

For an m_R of 3 ($m_R \times n = 3 \times 2 = 6$ grains), Fig. 20 (a) shows the number of bits plotted against the expected value of magnetization $E[M_{si}]$ averaged over one-row grains for the HC layer before and after LC writing.

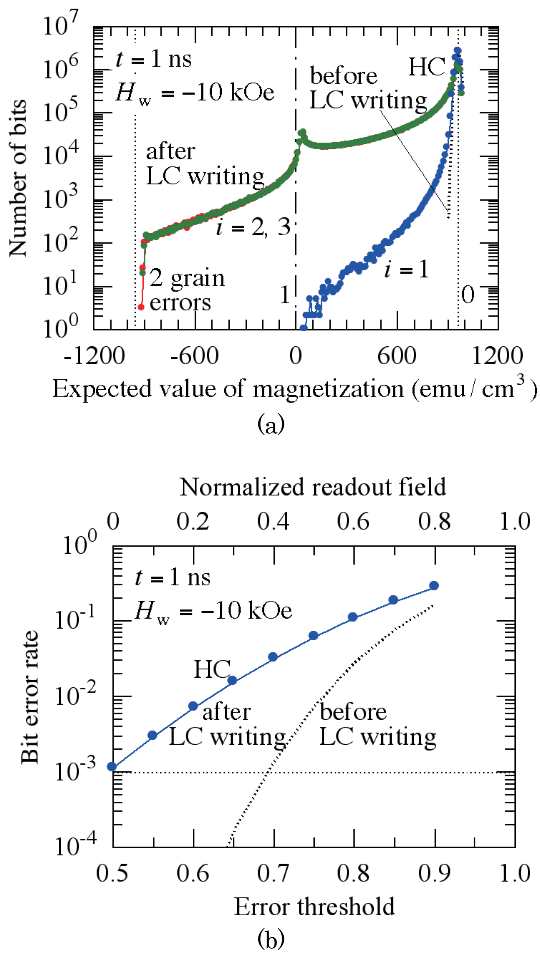

Fig. 20 (a) Number of bits plotted against expected value of magnetization $E[M_{si}]$ and (b) bit error rate for the HC layer as a function of error threshold E_{th} and normalized readout field H_0 before and after LC writing in 2 Tbpsi/layer 3D HAMR ($3 \times 2 = 6$ grains).

Table 14 LC writing in 2 Tbpsi/layer 3D HAMR (4 × 2 = 8 grains/bit).

	LC / HC	
	LC	HC
(LC writing)		
Minimum normalized readout field H_0		N / A
$D_{RT} \times H_0 \times H_{zpeak}$ (knmOe)		N / A

Significant information degradation can be seen in the 2nd (i = 2) and 3rd (i = 3) row grains when compared with the result shown in Fig. 13 (a), since the HC grain temperature during LC writing shown in Fig. 16 (b) is higher than that shown in Fig. 9 (b). Although the temperatures for the 1st and 2nd row grains in Fig. 9 (b) are 634 and 655 K, those for the 1st and 2nd (3rd) row grains in Fig. 16 (b) are 647 and 690 K, respectively. Temperature has a strong impact, since the T value is related to the $K_{ueff}(T)$ value and the denominator T in the $K_{ueff}(T)V/(kT)$, and $K_{ueff}(T)V/(kT)$ is a variable in the exponential function shown in Eq. (1). Accordingly, Fig. 20 (b) and Table 14 show that there is no E_{th} greater than 0.5, namely, no H_0 greater than 0 that satisfies a bER of 10^{-3} for the HC layer after LC writing.

A large bit aspect ratio is advantageous in terms of ATI and the $D_{RT} \times H_0 \times H_{zpeak}$ product. However, the information degradation in the HC layer during LC writing is large. Therefore, we believe that a small bit aspect ratio is preferable in 3D HAMR.

3.3.6 Writing sensitivity

The H_w dependence of the bER for the LC and HC layers is shown in Fig. 21. The writing sensitivity is also better than that for HAMR as shown in Fig. 5.

The reason for the difference between the bERs of the LC layers in Figs. 14 and 21 is that EAW is affected by the n values of 3 and 2, respectively. EAW can be suppressed by increasing the n value. On the other hand, the reasons for the difference between the bERs of the HC layers are the V values of 137 and 172 nm³ as shown in Tables 5 and 10, and that EAW is affected by the $\partial T_H/\partial y$ values of 8.8 and 11.3 K/nm as shown in Tables 6 and 11, respectively, as well as by the n values of 3 and 2. EAW can be suppressed by increasing the $\partial T_H/\partial y$ value.

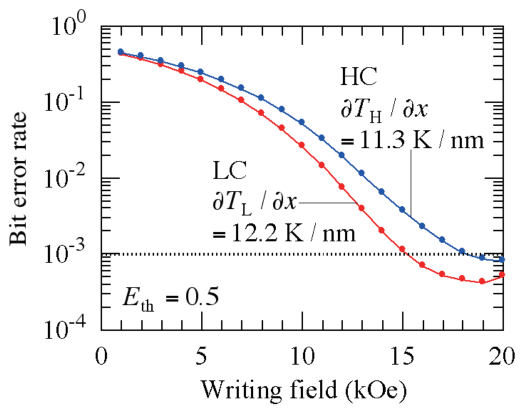

Fig. 21 Writing field H_w dependence of bit error rate in 2 Tbpsi/layer 3D HAMR (3 × 2 = 6 grains).

3.4 Comparison of shingled HAMR and 3D HAMR

We think the medium for comparison with 4 Tbpsi shingled HAMR is 2 Tbpsi/layer 3D HAMR with 3 × 3 = 9 grains/bit. The comparison results are summarized in Table 15.

(1) Grain aspect ratio

The $(h_{LC} + h_{HC})/D_m$ values for both HAMR and 3D HAMR may be too large to allow us to manufacture the recording layer.

(2) Mean Curie temperature

The low T_{LC} value of 650 K may be disadvantageous as regards the writing property, since the temperature dependence of the anisotropy field is somewhat smaller than that predicted by the theory.

Table 15 Comparison of 4 Tbpsi shingled HAMR (3 × 2 = 6 grains/bit) and 2 Tbpsi/layer 3D HAMR (3 × 3 = 9 grains/bit).

	Shingled HAMR	LC / HC	
		LC	HC
h (nm)	8.5	5.0	5.5
D_m (nm)	4.2	5.0	
σ_D / D_m (%)	15	15	
$(h_{LC} + h_{HC}) / D_m$	2.0	2.1	
V (nm³)	149	124	137
D_T (nm)	15.6	18.0	
D_B (nm)	10.4	18.0	
D_T / D_B	1.5	1.0	
K_u / K_{bulk}	0.8	0.8	
T_{cm} (K)	750	650	750
σ_{Tc} / T_{cm} (%)	2	2	
(Adjacent track interference)			
$m_R \times n$	2 × 2	2 × 3	2 × 3
D_{RT} (nm)	9.4	11.0	11.0
H_0	0.20	0.26	0.30
H_{zpeak} (Oe)	1197	1142	401
$D_{RT} \times H_0 \times H_{zpeak}$ (knmOe)	2.3	3.2	1.3
(10 yrs of archiving)			
$K_{ueff}V / (kT)$ (T = 350 K)	152	87	137
H_0	0.26	0.13	0.38
$D_{RT} \times H_0 \times H_{zpeak}$ (knmOe)	3.0	1.6	1.7
R_0	< 0.1	21	< 0.1
(LC writing)			
H_0			0.32
$D_{RT} \times H_0 \times H_{zpeak}$ (knmOe)			1.4
(Writing sensitivity)			
Bit error rate	High	Low	Low

(3) Readout property

In HAMR, the H_0 values are 0.20 and 0.26 for ATI and 10 years of archiving, respectively. Therefore, the limiting factor is ATI, since the grain pitch is small.

For the upper LC layer in 3D HAMR, the H_0 values are 0.26 and 0.13 for ATI and 10 years of archiving, respectively. Therefore, the limiting factor is 10 years of archiving, since the h_{LC} and/or T_{LC} values are small.

For the lower HC layer in 3D HAMR, the H_0 values of 0.30, 0.38, and 0.32 are large for ATI, 10 years of archiving, and LC writing, respectively. However, the $D_{RT} \times H_0 \times H_{zpeak}$ products are small, since the H_{zpeak} value of 401 Oe from the lower HC layer is small due to the limitation of thinning the upper LC layer related to the information stability in the LC layer. Therefore, the limiting factor is the H_{zpeak} value.

(4) Writing sensitivity

The bER for HAMR is higher than that for 3D HAMR. The reasons for the difference in bER are the statistical factor affected by the $m_R \times n$ value and EAW affected by the n value. This means that the writing sensitivity for HAMR is worse than that for 3D HAMR.

4. Conclusions

We compared 4 Tbpsi shingled HAMR and 2 Tbpsi/layer 3D HAMR.

Prior to the comparison, we examined the bit aspect ratio on 3D HAMR. A large bit aspect ratio is advantageous in terms of ATI and the readout property. However, there is considerable information degradation in the HC layer during LC writing. Therefore, we consider a small bit aspect ratio to be preferable in 3D HAMR.

For the upper LC layer in 3D HAMR, the minimum normalized readout field is small for 10 years of archiving, since the LC grain height and/or LC Curie temperature are small.

The peak z component of the readout field from the lower HC layer is small due to the limitation of thinning the upper LC layer related to the information stability in the LC layer.

The writing sensitivity for HAMR is worse than that for 3D HAMR because of a statistical factor affected by the readout grain number and erasure-after-write affected by the grain column number.

Although both HAMR and 3D HAMR have disadvantages, we think that the poor writing sensitivity in HAMR is a serious problem.

Acknowledgement We acknowledge the support of the Advanced Storage Research Consortium (ASRC), Japan.

References

1) Western Digital (private communication, December, 2018).
2) H. Yamane, S. J. Greaves, and Y. Tanaka: *IEEE Trans. Magn.,* **57**, 3200706-1-6 (2021).
3) T. Kobayashi, Y. Nakatani, and Y. Fujiwara: *J. Magn. Soc. Jpn.*, **45**, 16 (2021).
4) T. Kobayashi, Y. Nakatani, and Y. Fujiwara: *J. Magn. Soc. Jpn.*, **46**, 49 (2022).
5) M. Mansuripur and M. F. Ruane: *IEEE Trans. Magn.*, **MAG-22**, 33 (1986).
6) J. -U. Thiele, K. R. Coffey, M. F. Toney, J. A. Hedstrom, and A. J. Kellock: *J. Appl. Phys.*, **91**, 6595 (2002).
7) T. Kobayashi, Y. Isowaki, and Y. Fujiwara: *J. Magn. Soc. Jpn.*, **39**, 8 (2015).
8) T. Kobayashi, Y. Nakatani, and Y. Fujiwara: *J. Magn. Soc. Jpn.*, **44**, 122 (2020).
9) T. Kobayashi, Y. Nakatani, and Y. Fujiwara: *J. Magn. Soc. Jpn.*, **44**, 34 (2020).
10) E. D. Boerner and H. N. Bertram: *IEEE Trans. Magn.*, **34**, 1678 (1998).
11) T. Kobayashi, Y. Nakatani, and Y. Fujiwara: *J. Magn. Soc. Jpn.*, **46**, 10 (2022).
12) T. Kobayashi, Y. Nakatani, and Y. Fujiwara: *J. Magn. Soc. Jpn.*, **42**, 127 (2018).
13) Y. Kanai, Y. Jinbo, T. Tsukamoto, S. J. Greaves, K. Yoshida, and H. Muraoka: *IEEE. Trans. Magn.*, **46**, 715 (2010).
14) I. Suzuki, J. Wang, Y. K. Takahashi, and K. Hono: *J. Magn. Magn. Mat.*, **500**, 166418 (2020).
15) C. Xu, B. Zhou, T. Du, B. S. D. Ch. S. Varaprasad, D. E. Laughlin, and J. -G. Zhu: *APL Mat.*, **10**, 051105 (2022).
16) T. Kobayashi, Y. Isowaki, and Y. Fujiwara: *J. Magn. Soc. Jpn.*, **40**, 28 (2016).
17) T. Kobayashi, Y. Isowaki, and Y. Fujiwara: *J. Magn. Soc. Jpn.*, **43**, 70 (2019).

Received Aug. 22, 2022; Accepted Oct. 10, 2022

INDEX

J. Magn. Soc. Jpn., **47**, 15-19 (2023)

<Paper>

Synthesis and Analyses of Acicular Spinel Iron Oxide Particles with Core-Shell Structure Containing Manganese Ferrite and Magnetite

Sota Yamada[*], Mikio Kishimoto[*], and Hideto Yanagihara[*,**]
[*]Department of Applied Physics, Univ. of Tsukuba, *Tennodai 1-1-1, Tsukuba 305-8573, Japan*
[**] Tsukuba Research Center for Energy Materials Science (TREMS), Univ. of Tsukuba, *Tennodai 1-1-1, Tsukuba 305-8573, Japan*

Acicular spinel iron oxide particles with a core-shell structure containing manganese ferrite ($MnFe_2O_4$) and magnetite (Fe_3O_4) were synthesized by uniformly crystallizing $MnFe_2O_4$ on the surface of the magnetite particles in an alkaline dispersion. Crystallizing 50 wt% of $MnFe_2O_4$ on Fe_3O_4 led to an increase in the apparent lattice constant from 0.839 nm to 0.841 nm. Transmission electron microscopy (TEM) observations of the particle shape and lattice images showed that $MnFe_2O_4$ was uniformly crystallized on the surface of the magnetite particles and their acicular shape was maintained. The coercive force and saturation magnetization were almost constant at 29.5 kA/m and 80-81 Am^2/kg, respectively, when the crystallized $MnFe_2O_4$ content ranged from 0 to 30 wt%. When the $MnFe_2O_4$ content was increased to 50 wt%, the coercive force and saturation magnetization slightly decreased to approximately 28.0 kA/m and 74.1 Am^2/kg, respectively, reflecting the lower magnetization of $MnFe_2O_4$ compared to that of Fe_3O_4.

Key words: magnetic nanoparticles, core-shell structure, spinel ferrite

1. Introduction

There are many reports on particles synthesized with a core-shell structure that find applications in a variety of fields, such as electronics, biomedical, optics, and catalysis[1)-5)]. Among them, particles containing cobalt ferrite ($CoFe_2O_4$) are of particular interest from a practical standpoint due to the high magnetic anisotropy of $CoFe_2O_4$[6)-11)]. To synthesize particles with a core-shell structure containing $CoFe_2O_4$, precipitation methods have been reported to be effective for controlling the magnetic anisotropy[12),13)].

Several studies have investigated to improve the recording density of particulate magnetic recording tapes by increasing the coercive force through the addition of Co ions to spinel iron oxide particles[14)]. Initially, this was achieved by the substitution of Co ions in maghemite (γ-Fe_2O_3) particles[15)]. However, the magnetic anisotropy resulting from this method was cubic, whereas a uniaxial magnetic anisotropy is essential for recording tapes. To overcome this problem, particles with a core-shell structure were synthesized. In these particles, the $CoFe_2O_4$ layer was epitaxially crystallized on the surface of the seed γ-Fe_2O_3 particles with the same spinel structure[16)]. In this method, γ-Fe_2O_3 was reduced to magnetite (Fe_3O_4) in an alkaline dispersion.

The lattice constants of $CoFe_2O_4$ and Fe_3O_4 are close in value, at 0.838 and 0.839 nm, respectively. Therefore, we explored the possibility of epitaxially crystallizing another spinel oxide with a significantly different lattice constant from that of Fe_3O_4. Manganese ferrite ($MnFe_2O_4$) is known to possess the lattice constant of 0.851 nm, which is significantly different from that of Fe_3O_4. In this study, we tried to epitaxially or uniformly crystallize $MnFe_2O_4$ on the surface of acicular Fe_3O_4 particles, and examined the changes in the lattice constant, particle shape, and magnetic properties of the resulting acicular iron oxide particles with a core-shell structure containing $MnFe_2O_4$ and Fe_3O_4.

Corresponding author: Hideto Yanagihara (e-mail: yanagihara.hideto.fm@u.tsukuba.ac.jp).

2. Experimental procedures

2.1 Sample preparation

Commercially available acicular γ-Fe_2O_3 particles (Titan Kogyo, Ltd. AV-60) were used as the raw material. The Fe^{3+} ions in the γ-Fe_2O_3 particles were partially reduced to Fe^{2+} ions under a H_2 atmosphere at 300 °C for 2 h. Acicular iron oxide particles with a composition close to that of Fe_3O_4 were obtained, which were used as seed particles in this study.

$MnFe_2O_4$ was crystallized on the Fe_3O_4 particles as follows: One gram of Fe_3O_4 particles was dispersed in 100 mL of water using an ultrasonic disperser. Manganese chloride and ferrous chloride were dissolved in a 1:2 molar ratio in the above dispersion, following which three times the equivalent of sodium hydroxide required to form $Mn(OH)_2$ and $Fe(OH)_2$ was added under continuous stirring. The dispersion containing the Fe_3O_4 particle, $Mn(OH)_2$, and $Fe(OH)_2$ was treated hydrothermally in an autoclave at 110 °C for 24 h, where Fe^{2+} was oxidized to Fe^{3+}, and $MnFe_2O_4$ was crystallized in the dispersion. Using the above method, four samples containing different contents of $MnFe_2O_4$ were synthesized. In this report, the composition of the samples is defined as $MnFe_2O_4$(x wt%): Fe_3O_4(100- x wt%) (x =10, 20, 30, and 50). The expressed compositions of the samples are the amounts prepared upon the synthesis.

$MnFe_2O_4$ particles were prepared without the Fe_3O_4 seed particles using the above method in order to compare the particle shape with that of the core-shell-structured manganese ferrite particles (CSMPs) and magnetite particles.

2.2 Measurement

Transmission electron microscopy (TEM: JEN2010F, JEOL) was used to observe the shapes of the Fe_3O_4 particles, $MnFe_2O_4$ particles, and CSMPs, and lattice images were acquired to examine the crystal structure of the product formed on the CSMPs and magnetite particles.

X-ray diffraction (XRD; MiniFlex600, Rigaku) using CuKα radiation was conducted in the 2θ range of 20° - 60° for structural analyses. The lattice constants (a) of the CSMPs and magnetite particles were calculated from the d values of the 311 peak for each particle; this peak is the strongest peak in the spinel structure. This allowed the examination of the variation in the lattice due to the crystallization of $MnFe_2O_4$ on the surface of the Fe_3O_4 particles.

The particle size distribution was obtained by measuring the length and width of approximately one hundred particles on the corresponding TEM image. The data were used to examine the particle shape variation due to the crystallization of $MnFe_2O_4$ on the Fe_3O_4 particles.

The coercive force and saturation magnetization were measured using a vibrating sample magnetometer (TM-VSM2106-HGC, Tamakawa) under a maximum magnetic field of 1353 kA/m.

3. Results and discussion

3.1 Structural analyses

The XRD patterns measured in the 2θ range of 20° - 60° for the $MnFe_2O_4$ particles, Fe_3O_4 particles, and CSMPs (containing different content of $MnFe_2O_4$ in the range of 10 to 50 wt% with respect to Fe_3O_4) are shown in Figure 1. These patterns show typical peaks representative of iron oxides with a spinel structure. We note that the observed 311 peaks could be the combined 311 reflections of both $MnFe_2O_4$ and Fe_3O_4. The apparent lattice

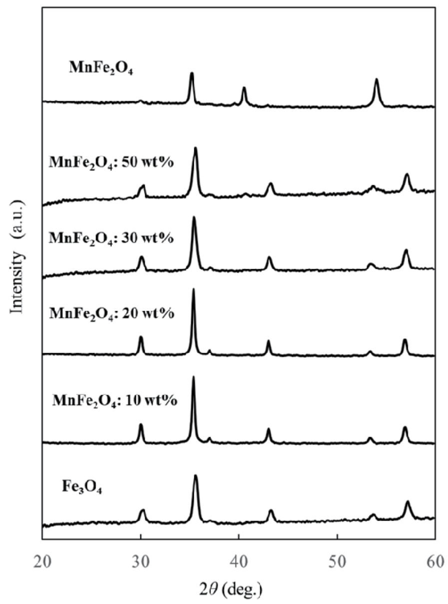

Fig. 1 XRD patterns measured in the 2θ range of 20 to 60 ° for $MnFe_2O_4$ particles, Fe_3O_4 particles, and crystallized $MnFe_2O_4$ (10 to 50 wt%) on the surface of Fe_3O_4 particles.

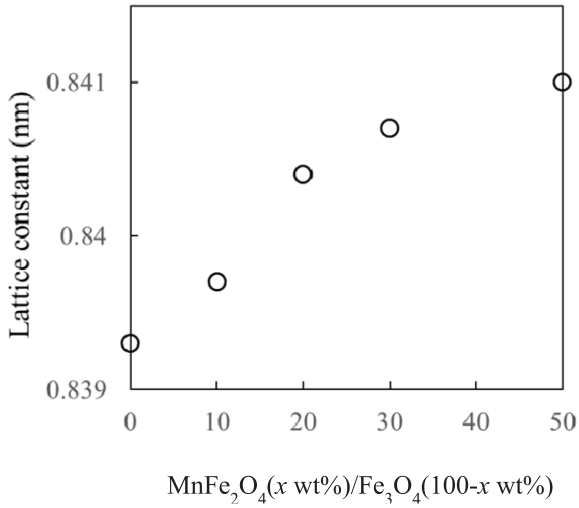

Fig. 2 Relationship between the crystallized $MnFe_2O_4$ content (ranging from 10 to 50 wt%) on the surface of Fe_3O_4 particles and the lattice constant.

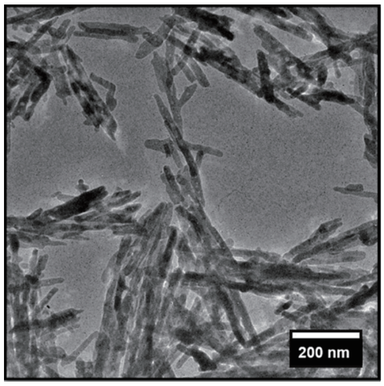

(a)

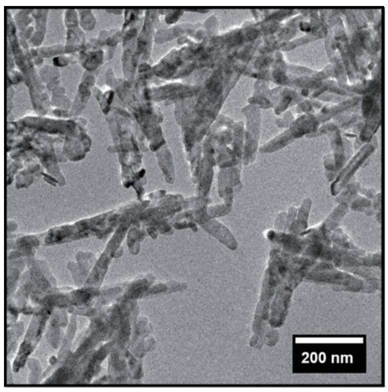

(b)

Fig. 3 TEM images of (a) Fe_3O_4 particles used as the seed particles and (b) crystallized 30 wt% $MnFe_2O_4$ on the surface of Fe_3O_4 particles.

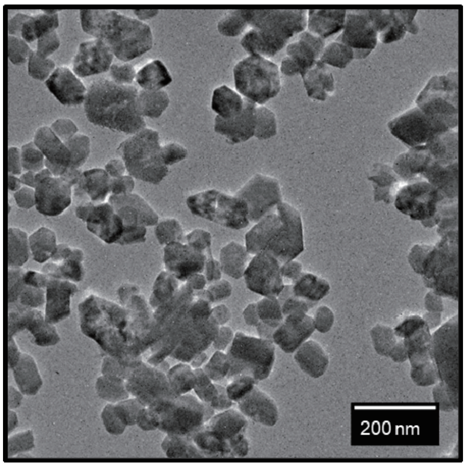

Fig. 4 TEM image of $MnFe_2O_4$ particles synthesized without Fe_3O_4 seed particles.

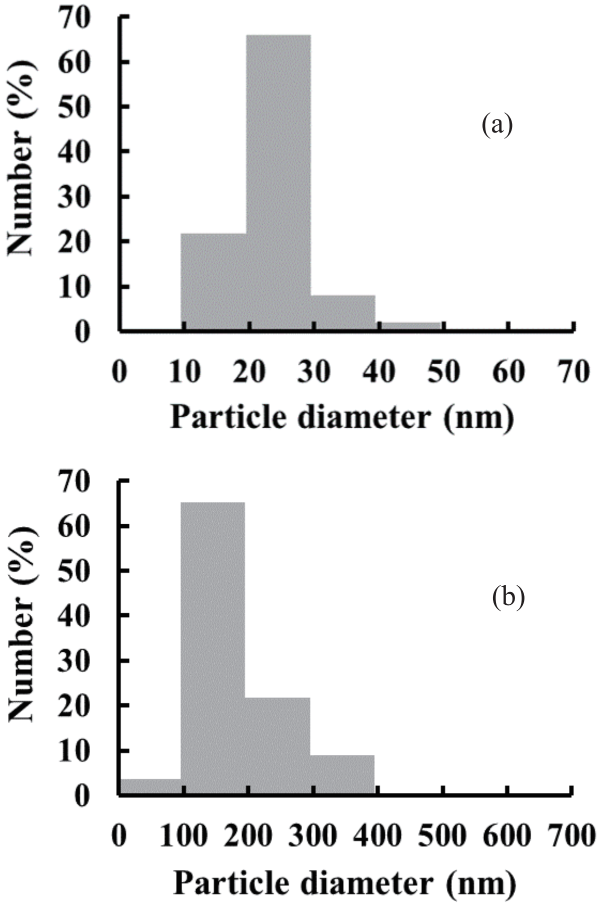

Fig. 5 Particle size distribution of Fe_3O_4 seed particles. The particle size distribution was obtained by measuring the (a) length and (b) width of approximately one hundred particles on the corresponding TEM image.

constants (a) of $MnFe_2O_4$ calculated from the d values of the 311 peak seems 0.846 nm, slightly lower than the value of 0.851 nm reported for bulk $MnFe_2O_4$.

Figure 2 shows the relationship between the $MnFe_2O_4$ content and apparent lattice constant of the respective

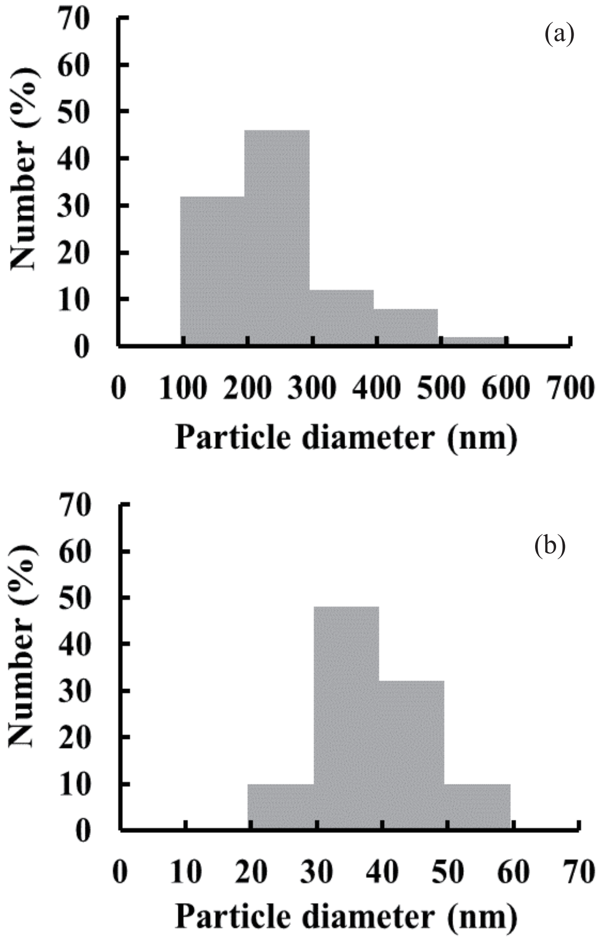

Fig. 6 Particle size distribution crystallized 30 wt% $MnFe_2O_4$ on Fe_3O_4 particles. The particle size distribution was obtained by measuring the (a) length and (b) width of approximately one hundred particles on the corresponding TEM image.

CSMPs. The apparent lattice constant of the CSMPs increased with increasing amount of $MnFe_2O_4$ from 0.839 nm in the Fe_3O_4 particles to 0.841 nm in the sample with 50 wt% $MnFe_2O_4$, reflecting the larger lattice constant of the crystallized $MnFe_2O_4$ compared to that of the Fe_3O_4 particles. Although the experimental error in the apparent lattice constant could be in the order of ~0.0005 nm, the apparent lattice constant appears to increase with increasing $MnFe_2O_4$ content, for which reproducibility was verified by several measurements.

3.2 Particle shapes and lattice images

The TEM images of the Fe_3O_4 particles used as seed particles and CSMPs crystallized with 30 wt% $MnFe_2O_4$ on the Fe_3O_4 particles are shown in Figures 3(a) and (b), respectively. Compared with the Fe_3O_4 particles, the CSMPs are clearly thicker because of the crystallization of $MnFe_2O_4$, while their acicular shapes were maintained. Figure 4 shows the TEM image of the $MnFe_2O_4$ particles synthesized without the seed Fe_3O_4 particles. The $MnFe_2O_4$ particles are hexagonal in shapes with a diameter of approximately 50 nm, which is distinctly different from those of CSMPs. These results show that the CSMPs have a core-shell structure in which $MnFe_2O_4$

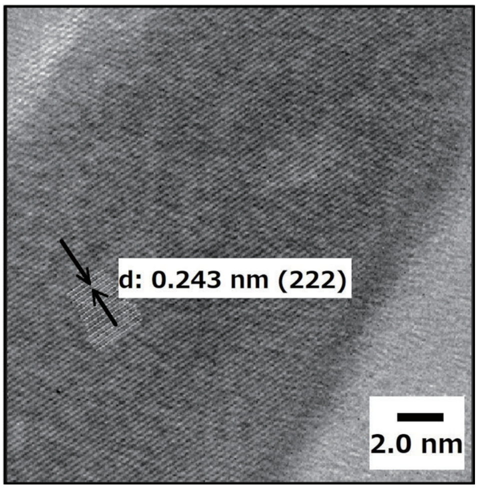

Fig. 7 Lattice image of crystallized 30 wt% $MnFe_2O_4$ on seed Fe_3O_4 seed particles.

is uniformly crystallized on the surface of the Fe_3O_4 particles.

3.3 Particle size distribution

The particle size distributions measured along the length and width of the Fe_3O_4 particles are shown in Figures 5(a) and (b), respectively. The median length and width are approximately 200 nm and 30 nm, respectively. Figures 6(a) and (b) show the particle size distribution measured along the length and width, respectively, of the CSMPs crystallized with 30 wt% $MnFe_2O_4$ on the Fe_3O_4 particles. The particle size distribution of the MCFPs is broader compared to that of the Fe_3O_4 particles due to the crystallization of $MnFe_2O_4$. The median length and width of the CSMPs are approximately 300 nm and 40-50 nm, respectively.

The lattice image of the CSMPs crystallized with 30 wt% $MnFe_2O_4$ on the Fe_3O_4 particles (as shown in Figure 3(b)) is shown in Figure 7. The lattice image is clear with a lattice spacing of 0.243 nm, which corresponds to that of the 222 peak in the spinel structure. The lattice constant calculated from the lattice spacing is 0.843 nm, which falls between the lattice constants for the Fe_3O_4 particles (0.839 nm) and $MnFe_2O_4$ particles (0.846 nm).

3.4 Magnetic properties

Figures 8 (a) and (b) show the relationship between the coercive force and saturation magnetization and the amount of $MnFe_2O_4$ in the CSMPs, respectively. The coercive force is approximately 29.5 kA/m, the same as that of the Fe_3O_4 particles with 10 to 30 wt% $MnFe_2O_4$ in the CSMPs, as shown in Figure 8 (a). When the amount of $MnFe_2O_4$ is increased to 50 wt%, the coercive force slightly decreases to approximately 28.0 kA/m. A similar dependency on the amount of $MnFe_2O_4$ is observed for the saturation magnetization, which remains 80-81 Am^2/kg in the range of 0 to 30 wt% $MnFe_2O_4$ in the CSMPs and decreases to 74.1 Am^2/kg for 50 wt% $MnFe_2O_4$, as shown in Figure 8 (b).

The coercive force in acicular particles depends on the shape magnetic anisotropy, which in turn is a function of the acicular ratio (ratio of the length and width of the particles) and the saturation magnetization. The almost-constant coercive force (Figure 8 (a)) is an indication that both, the acicular ratio and saturation magnetization, also do not change significantly with the use of 0 to 30 wt% $MnFe_2O_4$ in the CSMPs. The average acicular ratios calculated from the particle size distribution shown in Figures 5 and 6 are approximately 7 and 6 for the Fe_3O_4 particles and CSMPs with 30 wt% $MnFe_2O_4$, respectively. The almost- constant acicular ratio and saturation magnetization with 0 to 30 wt% $MnFe_2O_4$ in the CSMPs corresponds to the almost-constant coercive force in the same range of $MnFe_2O_4$ in the CSMPs. The significant decrease in the coercive force and magnetization at 50 wt% $MnFe_2O_4$ is attributed to the large amount of $MnFe_2O_4$, whose magnetization is significantly lower than that of the Fe_3O_4 particles.

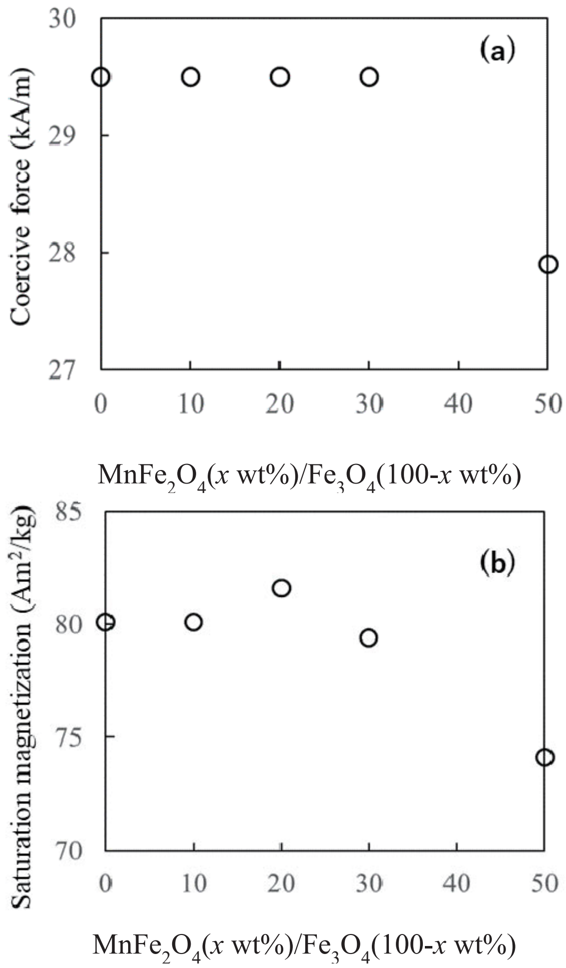

Fig. 8 Relationship between the (a) coercive force and (b) saturation magnetization, and crystallized $MnFe_2O_4$ content on Fe_3O_4 seed particles.

The results obtained from TEM and the magnetic properties indicate that $MnFe_2O_4$ is uniformly crystallized on the surface of Fe_3O_4 particles, preserving the acicular shape of the particles.

4. Conclusion

$MnFe_2O_4$ was uniformly crystallized on the surface of acicular Fe_3O_4 particles in an alkaline dispersion. TEM observations of the particle shape and the lattice images confirmed the uniform crystallization of $MnFe_2O_4$ on the

Fe_3O_4 particles. The lattice constant increased with the crystallization of $MnFe_2O_4$, reflecting the considerable difference between the lattice constants of $MnFe_2O_4$ and Fe_3O_4 particles. The coercive force and saturation magnetization were almost constant for 0 to 30 wt% $MnFe_2O_4$ and decreased at 50 wt% $MnFe_2O_4$, reflecting the smaller magnetization of $MnFe_2O_4$ compared to that of the Fe_3O_4 particles.

Acknowledgments This work was supported by the Japan Society for the Promotion of Science (JSPS) KAKENHI (Grant Number 20K21072). The TEM observations were performed using an equipment registered in the Open Facility System, University of Tsukuba.

References

1) A. López-Ortega, M. Estrader, G. Salazar-Alvarez, A. G. Roca, and J. Nogués: *Phys Rep.*, **553**,1 (2015).
2) R. G. Chaudhuri, and S. Paria: *Chem. Rev.*, **112**, 2373 (2012).
3) W. Schärtl: *Nanoscale*, **2**, 829 (2010).
4) H. Zeng, and S. Sun: *Adv. Funct. Mater.*, **18**, 391 (2008).
5) S. Behrens: *Nanoscale*, **3**, 877 (2011).
6) C. N. Chinnasamy, B. Jeyadevan, K. Shinoda, K. Tohji, D. J. Djayaprawira, M. Takahashi, R. J. Joseyphus, and A. Narayanasamy: *Appl. Phys. Lett.*, **83**, 2862 (2003).
7) V. Kumura, A. Rnaa, M. S. Yadav, and R. P. Pant: *J. Magn. Magn. Mater.*, **320**, 1729 (2008).
8) B. H. Liu, J. Ding, Z. L. Dong, C. B. Boothroyd, J. H. Yin, and J. B. Yi: *Phys. Rev. B*, **74**, 184427 (2006).
9) M. V. Limaye, S. B. Singh, S. K. Date, D. Kothari, V. R. Reddy, A. Gupta, V. Sathe, R. J. Choudhary, and S. K. Kulkarni: *J. Phys. Chem. B*, **113**, 9070 (2009).
10) K. Gandha, K. Elkins, N. Poudyal, and J. P. Liu: J. *Appl. Phys.*, **117**, 17A736 (2015).
11) D. Pal, M. Mandal, A. Chaudhuri, B. Das, D. Sarkar, and K. Mandal: *J. Appl. Phys.*, **108**, 124317 (2010).
12) D. Polishchuk, N. Nedelko, S. Solopan, A. Ś. Waniewska, V. Zamorskyi, A. Tovstolytkin and A. Belous: *Nanoscale Res. Lett.*, **13**, 1 (2018).
13) J. de A. Gomes, M. H. Sousa, F. A. Tourinho, R. Aquino, G. J. da Silva, J. Depeyrot, E. Dubois, and R. Perzynski: *J. Phys. Chem. C*, **112**, 6220 (2008).
14) A. A. van der Giessen: *Rev. Phys. Appl.*, **9**, 869 (1974).
15) G. Bate: *J. Magn. Magn. Mater.*, **100**, 413 (1991).
16) M. Kishimoto, M. Amemiya, and F. Hayama: *IEEE. Trans. Magn.*, **21**, 2626 (1985).

Received Apr. 19, 2022; Accepted Oct. 2, 2022

INDEX

J. Magn. Soc. Jpn., **47**, 20-17 (2023) <Paper>

Current-Induced Helicity Switching of Frustrated Skyrmions on a Square-Grid Obstacle Pattern

X. Zhang[1], J. Xia[1], O. A. Tretiakov[2], H. T. Diep[3], G. Zhao[4], J. Yang[5], Y. Zhou[6], M. Ezawa[7], and X. Liu[1]
[1]Department of Electrical and Computer Engineering, Shinshu University, *4-17-1 Wakasato, Nagano 380-8553, Japan*
[2]School of Physics, The University of New South Wales, *Sydney 2052, Australia*
[3]Laboratoire de Physique Théorique et Modélisation, CY Cergy Paris Université, *95302 Cergy-Pontoise Cedex, France*
[4]College of Physics and Electronic Engineering, Sichuan Normal University*, Chengdu 610068, China*
[5]State Key Laboratory for Mesoscopic Physics, School of Physics, Peking University, *Beijing, 100871, China*
[6]School of Science and Engineering, The Chinese University of Hong Kong, Shenzhen, *Guangdong 518172, China*
[7]Department of Applied Physics, The University of Tokyo, *7-3-1 Hongo, Tokyo 113-8656, Japan*

Topological spin textures on artificial pinning landscape may show unique static and dynamic properties. Here, we computationally show that the helicity of frustrated skyrmions on an artificial square-grid obstacle pattern can be switched by a spin current pulse. The obstacle pattern is formed by defect lines with enhanced perpendicular magnetic anisotropy, which could protect the skyrmion from being annihilated at the sample edge. It is found that the skyrmion driven by a moderate current shows a circular motion guided by the boundary of the obstacle pattern, while it shows an almost straight motion toward the sample edge in the absence of the obstacle pattern. By applying a short pulse current to drive the skyrmion in a sample with the obstacle pattern, we find that the helicity of the skyrmion could be switched between Bloch-type configurations favored by the dipole-dipole interaction. Besides, we demonstrate the possibility of switching the helicity of an array of skyrmions on the square-grid obstacle pattern using the same method. Our results could be useful for the helicity control of topological spin textures, and may provide guidelines for building future helicity-based spintronic functions.

Key words: magnetic skyrmion, frustrated spin system, helicity, obstacle, pinning, spintronics, micromagnetics

1. Introduction

Skyrmions were predicted theoretically to exist in magnetic materials more than three decades ago [1, 2], which are now in the vanguard of next-generation spintronic technologies [3-22]. They can be found in different types of magnetic materials [3-22], including chiral magnets and frustrated magnets. In chiral magnets, skyrmions are stabilized by the asymmetric exchange interaction [23-25], which is also called the Dzyaloshinskii-Moriya interaction [26, 27]. In frustrated magnets, skyrmions are stabilized by the exchange frustration induced by the competing exchange interactions [28-59]. The salient features of magnetic skyrmions include nanoscale size, low energy consumption, and most importantly, multiple degrees of freedom that can be controlled by external stimuli. Therefore, it is expected that skyrmions can be used as versatile building blocks in different information processing applications [3-22].

Most recently, it was suggested that frustrated skyrmions could be utilized as qubits in quantum computing [55, 60], where the manipulation of information is achieved through the precise control of the helicity degree of freedom. However, a frustrated skyrmion usually shows both center-of-mass and helicity dynamics when it is driven by an applied current [29, 30, 36, 42, 45, 57]. Namely, the helicity dynamics is coupled to the center-of-mass dynamics. Such a feature may limit the applications of frustrated skyrmions in helicity-based quantum computing and relevant devices. Hence, it is vital to find an effective way to control and manipulate the helicity degree of freedom of frustrated skyrmions. We note that the helicity state of a nanoscale skyrmion can be experimentally observed by using the Lorentz transmission electron microscopy (TEM) [61].

Possible solutions to avoid the translational motion of a frustrated skyrmion include the pinning of the skyrmion by an artificial defect and the geometric confinement of the skyrmion. For example, a ferromagnetic skyrmion in a nanodisk with the diameter close to the skyrmion diameter may show limited translational motion due to the confinement effect provided by the skyrmion-edge repulsion [62]. However, skyrmions could be destroyed by touching the edge. Recently, it has been shown that a more effective strategy to confine, protect, and control skyrmions in magnetic thin films is to construct defect lines with different magnetic properties [63-74], which can be realized in engineered multilayer nanostructures [75] or by using focused irradiation [76]. However, the helicity dynamics of a frustrated skyrmion confined by defect lines have not yet been explored. It is important to study such a problem, which is highly relevant to the realization of the skyrmion helicity-based applications.

In this work, we report the current-induced dynamics of isolated frustrated skyrmions on a square-grid obstacle pattern, which is made of orthogonal defect lines with

Corresponding author: Y. Zhou (e-mail: zhouyan@cuhk.edu.cn), M. Ezawa (e-mail: ezawa@ap.t.u-tokyo.ac.jp), X. Liu (e-mail: liu@cs.shinshu-u.ac.jp).

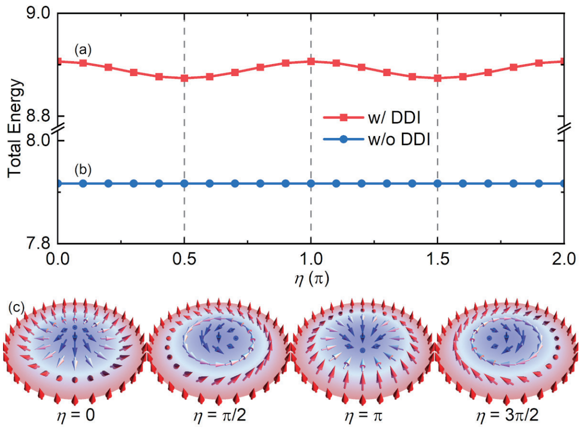

Fig. 1 The total energy of a frustrated skyrmion in the systems with or without the DDI. (a) The total energy of a frustrated skyrmion as a function of the helicity number η in the system with the DDI. The energies are given in units of $J_1 = 1$. (b) The total energy of a frustrated skyrmion as a function of the helicity number η in the system without the DDI. (c) Schematic illustration showing the spin configurations of skyrmions with the helicity numbers of $\eta = 0, \pi/2, \pi, 3\pi/2$. The out-of-plane spin component m_z is color coded: blue is into the plane, red is out of the plane, white is in-plane. The total energy is calculated by assuming a fixed helicity number η.

enhanced perpendicular magnetic anisotropy (PMA). We show that the helicity states of a single isolated frustrated skyrmion as well as an array of isolated frustrated skyrmions can be switched between Bloch-type configurations by a short current pulse. Our results could be a basis for future storage and computing device applications based on the manipulation of the helicity degree of freedom of topological spin textures.

2. Simulation and system

We focus on the dynamics of isolated skyrmions in a two-dimensional (2D) frustrated magnetic spin system, where the skyrmions are stabilized by a delicate competition among ferromagnetic nearest-neighbor (NN), antiferromagnetic next-NN (NNN), and antiferromagnetic next-NNN (NNNN) exchange interactions. The system is a J_1-J_2-J_3 classical Heisenberg model on a simple square lattice [30, 33, 36, 49]. The Hamiltonian $\mathcal{H}$ is given as

$$\begin{aligned}\mathcal{H} = &-J_1 \sum_{<i,j>} \boldsymbol{m}_i \cdot \boldsymbol{m}_j - J_2 \sum_{<<i,j>>} \boldsymbol{m}_i \cdot \boldsymbol{m}_j \\ &-J_3 \sum_{<<<i,j>>>} \boldsymbol{m}_i \cdot \boldsymbol{m}_j - K_\mathrm{u} \sum_i (m_i^z)^2 \\ &-\frac{1}{2} M_\mathrm{S} \sum_i \boldsymbol{B}_\mathrm{D} \cdot \boldsymbol{m}_i, \end{aligned} \qquad (1)$$

where $\boldsymbol{m}_i$ represents the normalized spin at the site i, $|\boldsymbol{m}_i| = 1$. $\langle i, j\rangle$, $\langle\langle i, j\rangle\rangle$, and $\langle\langle\langle i, j\rangle\rangle\rangle$ run over all the NN, NNN, and NNNN sites, respectively. J_1, J_2, and J_3 are the

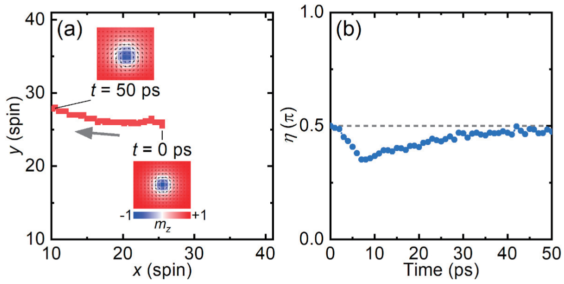

Fig. 2 Typical current-induced motion of a frustrated skyrmion in the system with the DDI. (a) A typical trajectory of a frustrated skyrmion in the system with the DDI, which shows the skyrmion moves almost straight toward the left edge of the sample. A relaxed skyrmion with $\eta = \pi/2$ is placed at the sample center as the initial state at $t = 0$ ps. The sample size is 51×51 spins. The skyrmion is driven by a current density of $j = 70$ MA/cm^2. The insets show the zoomed-in view of the skyrmion at $t = 0$ ps and $t = 50$ ps. Note that the insets only focus on the skyrmion texture instead of the whole sample. The arrow indicates the motion direction of the skyrmion. (b) The helicity of the skyrmion as a function of time during $t = 0 - 50$ ps. The skyrmion helicity slightly varies with time due to the current-induced deformation of the skyrmion during its motion toward the left sample edge. The skyrmion is annihilated by touching the left sample edge at $t = 66$ ps, where the skyrmion position and helicity cannot be tracked due to the significant deformation and annihilation.

constants for the NN, NNN, and NNNN Heisenberg exchange interactions, respectively. K_u is the easy-axis magnetic anisotropy constant, and the z-axis direction is defined as the easy axis. $\boldsymbol{B}_\mathrm{D}$ is the demagnetizing field resulting from the magnetic dipole-dipole interaction (DDI). M_S denotes the saturation magnetization. We note that we do not consider the interface-induced Dzyaloshinskii-Moriya interaction in this work as it could be suppressed for an ultrathin monolayer [77].

The spin dynamics is governed by the Landau-Lifshitz-Gilbert equation augmented with the damping-like spin-orbit torque [78-81],

$$\partial_t \boldsymbol{m} = -\gamma_0 \boldsymbol{m} \times \boldsymbol{h}_\mathrm{eff} + \alpha(\boldsymbol{m} \times \partial_t \boldsymbol{m}) + \boldsymbol{\tau}_\mathrm{d}, \qquad (2)$$

where t is the time, γ_0 is the absolute gyromagnetic ratio, and α is the Gilbert damping parameter. $\boldsymbol{h}_\mathrm{eff} = -\delta\mathcal{H}/(\delta\boldsymbol{m}\mu_0 M_\mathrm{S})$ is the effective field with μ_0 and ε being the vacuum permeability constant and average energy density, respectively. The saturation magnetization $M_\mathrm{S} = 580$ kA/m. The damping-like spin-orbit torque is expressed as $\boldsymbol{\tau}_\mathrm{d} = u\ (\boldsymbol{m} \times \boldsymbol{p} \times \boldsymbol{m})$, where the coefficient $u = |(\gamma_0 \hbar/\mu_0 e)|(j\theta_\mathrm{SH}/2aM_\mathrm{S})$. $\hbar$ is the reduced Planck constant, e is the electron charge, a is the sample thickness, j is the current density, and θ_SH is the spin Hall angle. The spin polarization direction $\boldsymbol{p} = +\hat{y}$. For the sake of simplicity, we assume that $\theta_\mathrm{SH} = 1$ so that the driving force is simply

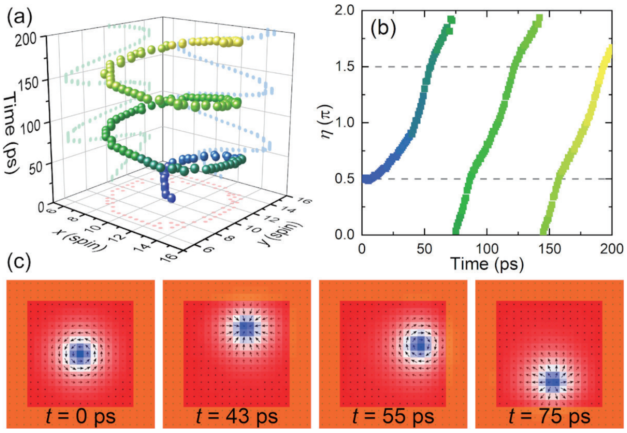

Fig. 3 Current-induced motion of a frustrated skyrmion in a sample with the obstacle pattern. (a) The trajectory of a frustrated skyrmion in a sample with the square-shaped obstacle pattern, which is formed by edge spins with enhanced PMA (i.e., K_o/K_u = 10 with K_o being the PMA of the obstacle defect line). A relaxed skyrmion with $\eta = \pi/2$ is placed at the sample center as the initial state at t = 0 ps. The skyrmion moves in an almost circular path guided by the obstacle pattern, which is driven by a current density of j = 40 MA/cm^2. The sample size is 21 × 21 spins. The width of the obstacle line is 3 spins. (b) The helicity of the skyrmion as a function of time during t = 0 − 200 ps. The skyrmion helicity changes between Bloch-type and Néel-type configurations during the motion of the skyrmion along the inner edge of the obstacle pattern. (c) Selected top-view snapshots showing the spin configurations of the skyrmion at t = 0, 43, 55, and 75 ps. The obstacle pattern with enhanced PMA is indicated by the orange area.

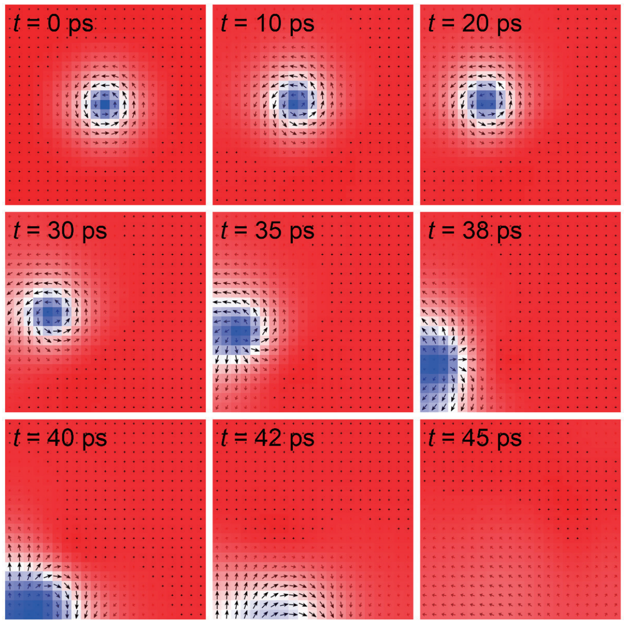

Fig. 4 Current-induced motion of a frustrated skyrmion in a sample without the obstacle pattern. Selected top-view snapshots showing the spin configurations of the frustrated skyrmion at t = 0, 10, 20, 30, 35, 38, 40, 42, and 45 ps in a sample without the obstacle pattern. A relaxed skyrmion with $\eta = \pi/2$ is placed at the sample center as the initial state at t = 0 ps. The sample size is 21×21 spins. The skyrmion is driven by a current density of j = 40 MA/cm^2. The skyrmion moves toward the sample edge and annihilates when touching the sample edge.

determined by j, i.e., $u \sim j$. In this work, we do not consider the effect of the field-like spin-orbit torque considering the helicity dynamics of a frustrated skyrmion is driven by the damping-like torque [30, 36)]. The simulation is done by using the Object Oriented MicroMagnetic Framework (OOMMF) [82)] upgraded with our extension modules for the J_1-J_2-J_3 classical Heisenberg model [30)]. In all simulations, the mesh size is a^3 with a = 0.4 nm being the lattice constant. Other default parameters are [30, 36, 45, 51, 52)]: J_1 = 30 meV, J_2 = −0.8 (in units of J_1 = 1), J_3 = −0.6 (in units of J_1 = 1), K_u = 0.02 (in units of J_1/a^3 = 1), α = 0.3, and $\gamma_0 = 2.211 \times 10^5$ m/(As).

3. Results and discussion

The helicity is an important degree of freedom of frustrated skyrmions, which can be used to perform helicity-based storage and computing. As shown in Fig. 1, we first review the total energy of a frustrated skyrmion as function of its helicity in the systems with or without the DDI. In the simulation, we first place a single isolated skyrmion with the skyrmion number of $Q = -1$ at the center of a sample with 21 × 21 spins with open boundary conditions in the x and y directions. The skyrmion number is defined as $Q = 1/4\pi \int \boldsymbol{m}\cdot(\partial_x\boldsymbol{m}\times\partial_y\boldsymbol{m})\mathrm{d}x\mathrm{d}y$. As the skyrmion can be parametrized as $\boldsymbol{m}(\boldsymbol{r}) = \boldsymbol{m}(\theta, \phi) = (\sin\theta\cos\phi, \sin\theta\sin\phi, \cos\theta)$, where $\phi = Q_v\varphi+\eta$ with φ being the azimuthal angle ($0 \leq \varphi < 2\pi$). Hence, the skyrmion considered in our work has a vorticity of $Q_v = \oint_C \mathrm{d}\phi/2\pi = +1$. $\eta \in [0, 2\pi)$ denotes the skyrmion helicity defined mod 2π. It can be seen that the total energy of a frustrated skyrmion depends on its helicity number η, where the Bloch-type configurations are favored by the DDI. Namely, the total energy of a frustrated skyrmion is independent of η only in the system without the DDI [see Fig. 1(b)]. Such a property is important for the dynamics of the frustrated skyrmion as the center-of-mass dynamics of frustrated skyrmions is coupled to the helicity dynamics [30)]. Namely, the skyrmion will move in a straight path with its helicity being fixed at the energetically favored Bloch-type configurations (i.e., $\eta = \pi/2, 3\pi/2$) in the system with the DDI [36)].

Therefore, in order to switch the helicity of a frustrated skyrmion in the system with the DDI, one will need to apply a driving current larger than a critical value to induce the helicity switching when the skyrmion can overcome the energy barrier between two different Bloch-type configurations [36)]. However, the critical value of the driving current density could be high, although the DDI-induced energy barrier may be reduced by reducing the value of the saturation magnetization. Note that the skyrmion stability may also be dependent on the saturation magnetization. Meanwhile, the position of the skyrmion may not be controlled due to the center-of-mass motion coupled to the helicity dynamics [36]. For example, in Fig. 2 we show the current-induced dynamics of a frustrated skyrmion at a moderate driving current density in the system with the DDI, where the skyrmion with Bloch-type helicity moves in an almost straight path toward the left edge of the sample. The trajectory and time-dependent helicity number of the skyrmion are given in Figs. 2(a) and 2(b), respectively. The skyrmion will be annihilated when it touches the edge of the sample. Hence, we propose an effective way to protect the frustrated skyrmion from being annihilated at the sample edge, and at the same time, to realize the current-induced switching of the skyrmion helicity in the system with the DDI.

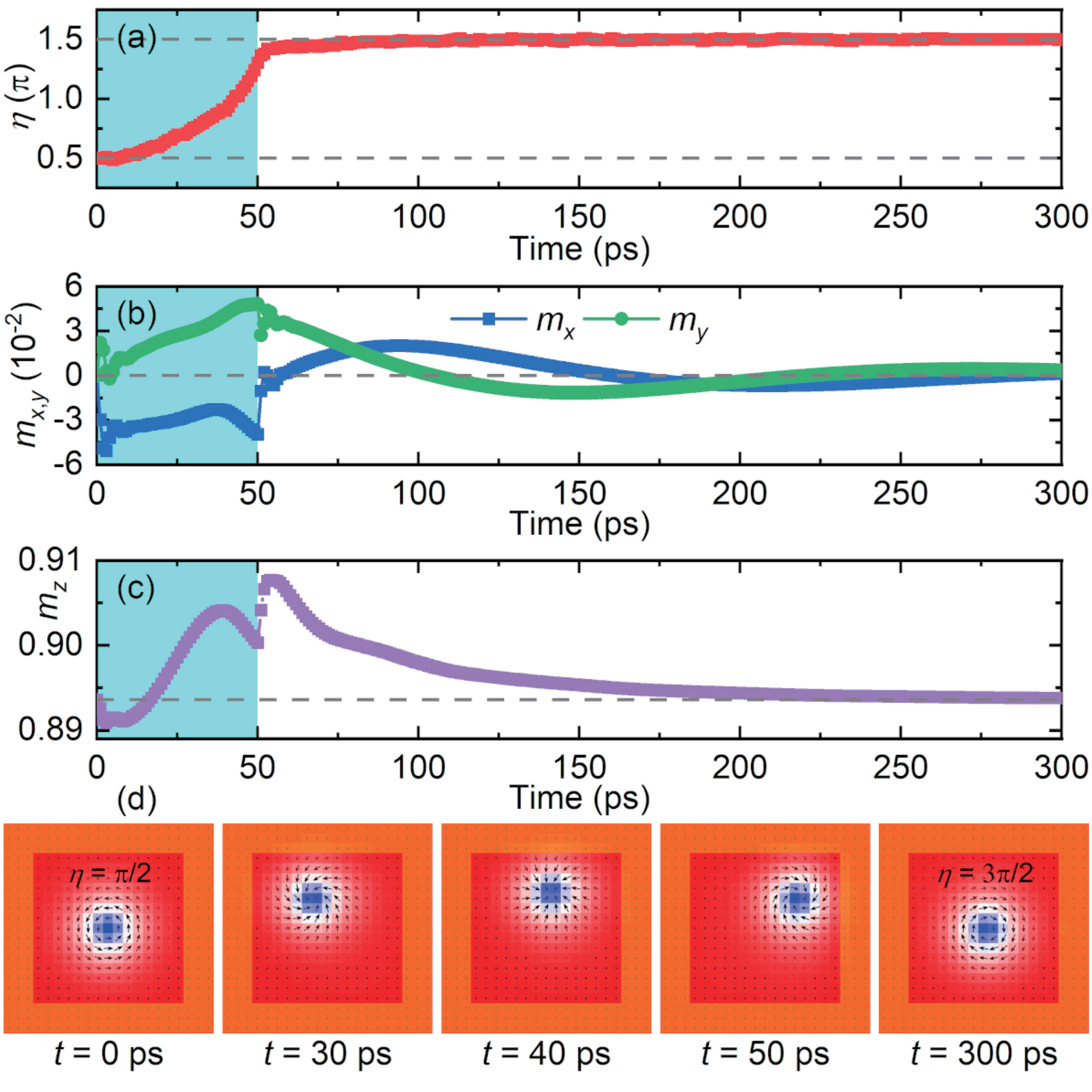

Fig. 5 Helicity switching of a frustrated skyrmion in a sample with the obstacle pattern induced by a short current pulse. (a) The helicity of the skyrmion as a function of time during $t = 0 - 300$ ps. A relaxed skyrmion with $\eta = \pi/2$ is placed at the sample center as the initial state at $t = 0$ ps. The skyrmion is driven by a current density of $j = 40$ MA/cm^2 for 50 ps, followed by a relaxation of 250 ps. The sample size is 21 × 21 spins. The width of the obstacle line is 3 spins. The obstacle has an enhanced PMA (i.e., $K_o/K_u = 10$). The skyrmion helicity switches from $\eta = \pi/2$ to $\eta = 3\pi/2$ after the application of the current pulse. (b) The in-plane spin components $m_{x,y}$ as functions of time during $t = 0 - 300$ ps. (c) The out-of-plane spin components m_z as a function of time during $t = 0 - 300$ ps. Note that m_x, m_y, and m_z are the normalized in-plane and out-of-plane spin components for the whole sample. (d) Selected top-view snapshots showing the spin configurations of the skyrmion at $t = 0$, 30, 40, 50, and 300 ps. The obstacle pattern with enhanced PMA is indicated by the orange area.

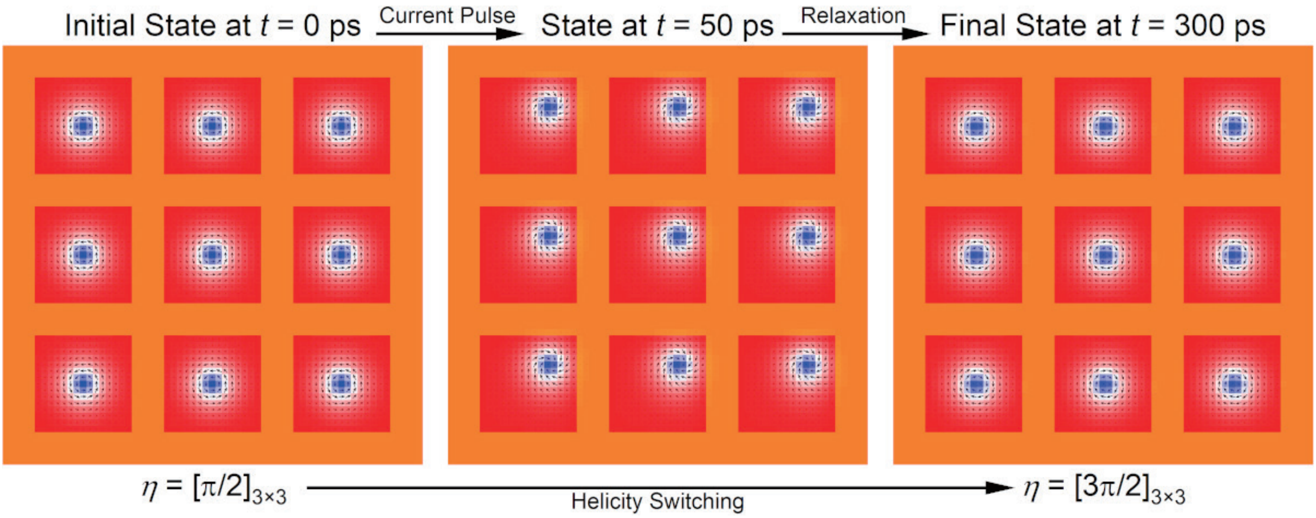

Fig. 6 Helicity switching of an array of nine frustrated skyrmions in a sample with the square-grid obstacle pattern induced by a short current pulse. Selected top-view snapshots showing the spin configurations of the frustrated skyrmions at $t = 0$, 50, and 300 ps. Nine relaxed skyrmions with $\eta = \pi/2$ are placed in the sample as the initial state at $t = 0$ ps. The system is driven by a current density of $j = 40$ MA/cm^2 for 50 ps, followed by a relaxation of 250 ps. The sample size is 65 × 65 spins. The width of the obstacle line is 5 spins. The obstacle has an enhanced PMA (i.e., $K_o/K_u = 10$). The helicity of all skyrmions switch from $\eta = \pi/2$ to $\eta = 3\pi/2$ after the application of the current pulse. The obstacle pattern with enhanced PMA is indicated by the orange area.

As shown in Fig. 3, we first study the dynamics of a single isolated frustrated skyrmion driven by a moderate current of $j = 40$ MA/cm^2. The system is a sample of 21 × 21 spins, where an obstacle pattern is formed by defect lines at the four edges. We assume that the obstacle pattern has an enhanced PMA, i.e., $K_o/K_u = 10$, which could be realized by locally modifying the PMA in principle. Note that we assumed a large value of K_o/K_u in order to make sure that the skyrmion cannot penetrate the obstacle. In real experiments, it is unnecessary to realize a large value of K_o/K_u. The width of the defect line is set to 3 spins. As the PMA of the obstacle area is larger than that in the interior of the sample, the skyrmion-obstacle interaction provides a repulsive force, which avoids the skyrmion penetrating the boundary of the obstacle. Such a feature also protects the skyrmion from be touching the edge of the sample, which may result in a better dynamic stability in the sample. It can be seen that the skyrmion moves in a circular path driven by the current and guided by the inner boundary of the obstacle pattern [see Fig. 3(a)]. We note that the skyrmion dynamics is affected by the obstacle pattern as soon as the current is applied, because the obstacle is initially very close to the skyrmion. Namely, the skyrmion is tightly confined by the obstacle pattern. When the obstacle is initially far from the skyrmion, the skyrmion should, in principle, first move to the left with a fixed helicity [see Fig. 2(a)] and then perform the circular motion with varying helicity when it is close to and guided by the obstacle.

As the helicity dynamics is coupled to the center-of-mass dynamics of the skyrmion [30], the helicity of the skyrmion also varies with time during the circular motion of the skyrmion, as shown in Fig. 3(b). In Fig. 3(c), we also show some selected top-view snapshots of the spin configurations of the sample, which show that the skyrmion helicity varies between Bloch-type and Néel-type configurations although the Bloch-type ones are favored by the DDI. As long as the driving current is applied, the skyrmion will move in the circular path with a varying helicity. However, it should be noted that the skyrmion driven by the same current of $j = 40$ MA/cm^2 will move toward the left edge and get annihilated from the edge in the sample without the obstacle pattern, as shown in Fig. 4. Namely, the circular motion and helicity switching of the skyrmion are a result of the skyrmion-obstacle interaction. We also note that the helicity switching is mainly controlled by the driving current, the dipole-dipole interaction, and the skyrmion-obstacle interaction. The frustrated skyrmion is stabilized by the exchange frustration instead of the asymmetric exchange interaction (i.e., the Dzyaloshinskii-Moriya interaction). The exchange frustration is realized by a delicate competition between different exchange interactions, therefore, the NNN and NNNN exchange interactions may affect the stability of the skyrmion. However, they may not affect the switching of the skyrmion helicity.

Based on the current-induced dynamic behaviors of a frustrated skyrmion in a sample with the obstacle pattern, we show in Fig. 5 that it is possible to switch the helicity of a frustrated skyrmion between the Bloch-type configurations favored by the DDI, i.e., $\eta = \pi/2 \rightarrow 3\pi/2$. To switch the skyrmion helicity, we apply a short current pulse to drive the dynamics of a single isolated frustrated skyrmion in a sample with the obstacle pattern. The geometry and other system settings are the same as that used in the simulation in Fig. 3. The current density is j = 40 MA/cm^2 and the pulse length is τ = 50 ps. The pulse length is determined based on the result given in Fig. 3(b). After the application of a single current pulse, the system is relaxed for 250 ps. Namely, the total simulation time is 300 ps. It can be seen in Fig. 5(a) that the helicity of the skyrmion varies from $\eta = \pi/2$ to $\eta =\sim 3\pi/2$ during the application of the current pulse (i.e., t = 0 – 50 ps). When the current is off, the helicity of the skyrmion approaches $\eta = 3\pi/2$ during the relaxation and finally remains as $\eta = 3\pi/2$ at t = 300 ps. Namely, the helicity of the skyrmion is switched from the Bloch-type configuration $\eta = \pi/2$ to the other Bloch-type configuration $\eta = 3\pi/2$ after the application of a 50-ps-long current pulse.

In Figs. 5(b) and 5(c), we show the time-dependent in-plane and out-of-plane spin components of the system during the helicity switching and relaxation of the system. It shows that the system responds to the driving current instantly during t = 0 − 50 ps and then relatively slowly relaxes to the energetically favored state during t = 50 − 300 ps. In Fig. 5(d), we show several selected top-view snapshots of the spin configurations of the sample. It can be seen that the skyrmion shows opposite Bloch-type helicities at the initial and final states. Namely, the skyrmion helicity is changed from the initial value $\eta = \pi/2$ to $\eta = 3\pi/2$ at the final state.

In Fig. 6, we further demonstrate that it is possible to switch the helicity of an array of frustrated skyrmions between the Bloch-type configurations on a square-grid obstacle pattern. The system is a sample of 65 × 65 spins, where an obstacle pattern is formed by orthogonal defect lines. The width of the defect line is set to 5 spins. Hence, the distance between two nearest-neighboring parallel defect lines is 15 spins. The geometry and other system settings are the same as that used in the simulation in Fig. 3. It should be noted that the width of the defect line will not affect the results as we assumed a strong anisotropy for the defect line in this work for the sake of simplicity, i.e., the skyrmion cannot penetrate the defect-line obstacle.

We put nine relaxed skyrmions with $\eta = \pi/2$ in the sample as the initial state at t = 0 ps. To switch the skyrmion helicity, we apply a short current pulse to drive the system. The current pulse profile is the same as that used in Fig. 5, i.e., the current density is j = 40 MA/cm^2 and the pulse length is τ = 50 ps. After the application of a single current pulse, the system is relaxed for 250 ps. As shown in Fig. 6, the helicity numbers of the nine skyrmions are switched from $\eta = \pi/2$ to $\eta = 3\pi/2$ in a uniform manner induced by the current pulse. We note that the nine skyrmions are far enough from each other, and the applied spin current is uniform in the whole sample. As a result, each skyrmion can be treated as an isolated skyrmion, and the dipole-dipole interaction will not lead to different dynamics for different skyrmions. Namely, the dynamics of each skyrmion is similar to the helicity switching

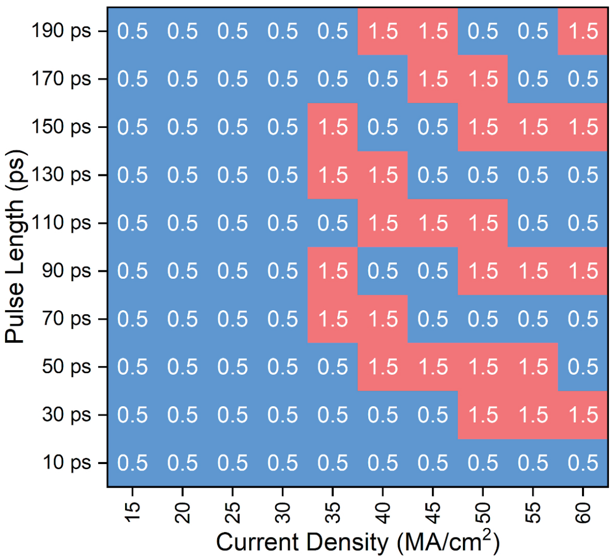

Fig. 7 A phase diagram showing the helicity switching of a frustrated skyrmion induced by a short current pulse in a sample with the obstacle pattern. A relaxed skyrmion with $\eta = \pi/2$ is placed at the sample center as the initial state at t = 0 ps. The skyrmion is driven by a current pulse, followed by a relaxation until t = 500 ps. The sample size is 21 × 21 spins. The width of the obstacle line is 3 spins. The obstacle has an enhanced PMA (i.e., K_o/K_u = 10). The number in the phase diagram indicates the relaxed skyrmion helicity (in units of π) after the application of the current pulse.

dynamics of a single skyrmion given in Fig. 5. Therefore, in principle, it is possible to switch the helicity of an array of many skyrmions in a large-scale sample with the square-grid obstacle pattern. Such an array of many skyrmions may be useful for building skyrmion-based multistate memory devices.

We also point out that the current-induced switching process of the skyrmion helicity on the obstacle pattern depends on the applied current density and pulse length. As shown in Fig. 7, for higher current density, the minimum required pulse length to switch the helicity could be reduced. Namely, for lower current density, the minimum required pulse length to switch the helicity may be increased. However, when the current density is smaller than 30 MA/cm^2, the skyrmion helicity cannot be switched, indicating there is a critical current density beyond which the helicity switching can be achieved.

4. Conclusion

In conclusion, we have investigated the current-induced dynamics of a frustrated skyrmion in a sample with or without the obstacle pattern. The obstacle pattern with enhanced PMA could provide the skyrmion from being annihilated at the sample edge due to the skyrmion-obstacle repulsion, and more importantly, could lead to the circular motion of the frustrated skyrmion with time-varying helicity driven by a moderate current density. Namely, the repulsive interaction between the skyrmion and the defect-line obstacle plays an important role in the helicity dynamics of the skyrmion. In the system without the obstacle pattern, the frustrated skyrmion will move with a fixed Bloch-type helicity due to the DDI and may be annihilated at the sample edge. We have also studied the current-induced helicity switching of a single frustrated skyrmion in a sample with the obstacle pattern, where we find that the helicity of the skyrmion can be switched from a Bloch-type configuration to the other Bloch-type configuration driven by a short current pulse. In addition, we show that the current-induced switching of the skyrmion helicity can be realized for an array of frustrated skyrmions on a square-grid obstacle pattern. Our results suggest that the helicity degree of freedom of topological spin textures may be effectively controlled on nanostructures with well-designed obstacle patterns. Our results also show the possibility that the helicity of skyrmions may be used in spintronic functions.

Acknowledgements X.Z. was a JSPS International Research Fellow supported by JSPS KAKENHI (Grant No. JP20F20363). J.X. was a JSPS International Research Fellow supported by JSPS KAKENHI (Grant No. JP22F22061). O.A.T. acknowledges support from the Australian Research Council (Grant No. DP200101027), Russian Science Foundation (Grant No. 21-42-00035), NCMAS grant, and the Cooperative Research Project Program at the Research Institute of Electrical Communication, Tohoku University. G.Z. acknowledges support from the National Natural Science Foundation of China (Grants No. 51771127, No. 52171188, and No. 52111530143). J.Y. acknowledges support from the National Natural Science Foundation of China (Grant No. 51731001). Y.Z. acknowledges support from the Guangdong Special Support Project (Grant No. 2019BT02X030), Shenzhen Fundamental Research Fund (Grant No. JCYJ20210324120213037), Shenzhen Peacock Group Plan (Grant No. KQTD20180413181702403), Pearl River Recruitment Program of Talents (Grant No. 2017GC010293), and National Natural Science Foundation of China (Grants No. 11974298, No. 12004320, and No. 61961136006). M.E. acknowledges support from the Grants-in-Aid for Scientific Research from JSPS KAKENHI (Grants No. JP18H03676 and No. JP17K05490) and support from CREST, JST (Grants No. JPMJCR20T2 and No. JPMJCR16F1). X.L. acknowledges support by the Grants-in-Aid for Scientific Research from JSPS KAKENHI (Grants No. JP20F20363, No. JP21H01364, No. JP21K18872, and No. JP22F22061).

References

1) A. N. Bogdanov and D. A. Yablonskii: *Sov. Phys. JETP*, **68**, 101 (1989).
2) U. K. Rößler, A. N. Bogdanov, and C. Pfleiderer: *Nature*, **442**, 797 (2006).
3) N. Nagaosa and Y. Tokura: *Nat. Nanotechnol.*, **8**, 899 (2013).
4) M. Mochizuki and S. Seki: *J. Phys.: Condens. Matter*, **27**, 503001 (2015).
5) R. Wiesendanger: *Nat. Rev. Mater.*, **1**, 16044 (2016).
6) G. Finocchio, F. Büttner, R. Tomasello, M. Carpentieri, and M. Kläui: *J. Phys. D: Appl. Phys.*, **49**, 423001 (2016).
7) W. Kang, Y. Huang, X. Zhang, Y. Zhou, and W. Zhao: *Proc. IEEE*, **104**, 2040 (2016).
8) N. Kanazawa, S. Seki, and Y. Tokura: *Adv. Mater.*, **29**, 1603227 (2017).
9) W. Jiang, G. Chen, K. Liu, J. Zang, S. G. E. te Velthuis, and A. Hoffmann: *Phys. Rep.*, **704**, 1 (2017).
10) A. Fert, N. Reyren, and V. Cros: *Nat. Rev. Mater.*, **2**, 17031 (2017).
11) K. Everschor-Sitte, J. Masell, R. M. Reeve, and M. Kläui: *J. Appl. Phys.*, **124**, 240901 (2018).
12) A. N. Bogdanov and C. Panagopoulos: *Nat. Rev. Phys.*, **2**, 492 (2020).
13) X. Zhang, Y. Zhou, K. Mee Song, T.-E. Park, J. Xia, M. Ezawa, X. Liu, W. Zhao, G. Zhao, and S. Woo: *J. Phys.: Condens. Matter*, **32**, 143001 (2020).
14) Y. Fujishiro, N. Kanazawa, and Y. Tokura: *Appl. Phys. Lett.*, **116**, 090501 (2020).
15) C. Back, V. Cros, H. Ebert, K. Everschor-Sitte, A. Fert, M. Garst, T. Ma, S. Mankovsky, T. L. Monchesky, M. Mostovoy, N. Nagaosa, S. S. P. Parkin, C. Pfleiderer, N. Reyren, A. Rosch, Y. Taguchi, Y. Tokura, K. von Bergmann, and J. Zang: *J. Phys. D: Appl. Phys.*, **53**, 363001 (2020).
16) B. Göbel, I. Mertig, and O. A. Tretiakov: *Phys. Rep.*, **895**, 1 (2021).
17) S. Li, W. Kang, X. Zhang, T. Nie, Y. Zhou, K. L. Wang, and W. Zhao: *Mater. Horiz.*, **8**, 854 (2021).
18) S. Luo and L. You: *APL Mater.*, **9**, 050901 (2021).
19) Y. Tokura and N. Kanazawa: *Chem. Rev.*, **121**, 2857 (2021).
20) H. Vakili, J.-W. Xu, W. Zhou, M. N. Sakib, M. G. Morshed, T. Hartnett, Y. Quessab, K. Litzius, C. T. Ma, S. Ganguly, M. R. Stan, P. V. Balachandran, G. S. D. Beach, S. J. Poon, A. D. Kent, and A. W. Ghosh: *J. Appl. Phys.*, **130**, 070908 (2021).
21) C. H. Marrows and K. Zeissler: *Appl. Phys. Lett.*, **119**, 250502 (2021).
22) C. Reichhardt, C. J. O. Reichhardt, and M. V. Milošević: *Rev. Mod. Phys.*, **94**, 035005 (2022).
23) S. Mühlbauer, B. Binz, F. Jonietz, C. Pfleiderer, A. Rosch, A. Neubauer, R. Georgii, and P. Böni: *Science*, **323**, 915 (2009).
24) X. Z. Yu, Y. Onose, N. Kanazawa, J. H. Park, J. H. Han, Y. Matsui, N. Nagaosa, and Y. Tokura: *Nature*, **465**, 901 (2010).
25) S. Heinze, K. von Bergmann, M. Menzel, J. Brede, A. Kubetzka, R. Wiesendanger, G. Bihlmayer, and S. Blügel: *Nat. Phys.*, **7**, 713 (2011).
26) I. Dzyaloshinskii: *J. Phys. Chem. Solids*, **4**, 241 (1958).
27) T. Moriya: *Phys. Rev.*, **120**, 91 (1960).
28) T. Okubo, S. Chung, and H. Kawamura: *Phys. Rev. Lett.*, **108**, 017206 (2012).
29) A. O. Leonov and M. Mostovoy: *Nat. Commun.*, **6**, 8275 (2015).
30) S.-Z. Lin and S. Hayami: *Phys. Rev. B*, **93**, 064430 (2016).

31) S. Hayami, S.-Z. Lin, and C. D. Batista: *Phys. Rev. B*, **93**, 184413 (2016).
32) L. Rozsa, A. Deak, E. Simon, R. Yanes, L. Udvardi, L. Szunyogh, and U. Nowak: *Phys. Rev. Lett.*, **117**, 157205 (2016).
33) C. D. Batista, S.-Z. Lin, S. Hayami, and Y. Kamiya: *Rep. Prog. Phys.*, **79**, 084504 (2016).
34) A. O. Leonov and M. Mostovoy: *Nat. Commun.*, **8**, 14394 (2017).
35) Y. A. Kharkov, O. P. Sushkov, and M. Mostovoy: *Phys. Rev. Lett.*, **119**, 207201 (2017).
36) X. Zhang, J. Xia, Y. Zhou, X. Liu, H. Zhang, and M. Ezawa: *Nat. Commun.*, **8**, 1717 (2017).
37) H. Y. Yuan, O. Gomonay, and M. Kläui: *Phys. Rev. B*, **96**, 134415 (2017).
38) Y. Hu, X. Chi, X. Li, Y. Liu, and A. Du: *Sci. Rep.*, **7**, 16079 (2017).
39) S. von Malottki, B. Dupe, P. F. Bessarab, A. Delin, and S. Heinze: *Sci. Rep.*, **7**, 12299 (2017).
40) A. Sonntag, J. Hermenau, S. Krause, and R. Wiesendanger: *Phys. Rev. Lett.*, **113**, 077202 (2014).
41) J. J. Liang, J. H. Yu, J. Chen, M. H. Qin, M. Zeng, X. B. Lu, X. S. Gao, and J. M. Liu: *New J. Phys.*, **20**, 053037 (2018).
42) U. Ritzmann, S. von Malottki, J.-V. Kim, S. Heinze, J. Sinova, and B. Dupé: *Nat. Electron.*, **1**, 451 (2018).
43) T. Kurumaji, T. Nakajima, M. Hirschberger, A. Kikkawa, Y. Yamasaki, H. Sagayama, H. Nakao, Y. Taguchi, T.-h. Arima, and Y. Tokura: *Science*, **365**, 914 (2019).
44) L. Desplat, J. V. Kim, and R. L. Stamps: *Phys. Rev. B*, **99**, 174409 (2019).
45) J. Xia, X. Zhang, M. Ezawa, Z. Hou, W. Wang, X. Liu, and Y. Zhou: *Phys. Rev. Applied*, **11**, 044046 (2019).
46) R. Zarzuela, H. Ochoa, and Y. Tserkovnyak: *Phys. Rev. B*, **100**, 054426 (2019).
47) V. Lohani, C. Hickey, J. Masell, and A. Rosch: *Phys. Rev. X.*, **9**, 041063 (2019).
48) B. Göbel, A. Mook, J. Henk, I. Mertig, and O. A. Tretiakov: *Phys. Rev. B*, **99**, 060407(R) (2019).
49) T. H. Diep: *Entropy*, **21**, 175 (2019).
50) I. F. Sharafullin and H. T. Diep: *Symmetry*, **12**, 26 (2020).
51) X. Zhang, J. Xia, L. Shen, M. Ezawa, O. A. Tretiakov, G. Zhao, X. Liu, and Y. Zhou: *Phys. Rev. B*, **101**, 144435 (2020).
52) J. Xia, X. Zhang, M. Ezawa, O. A. Tretiakov, Z. Hou, W. Wang, G. Zhao, X. Liu, H. T. Diep, and Y. Zhou: *Appl. Phys. Lett.*, **117**, 012403 (2020).
53) X. Zhang, J. Xia, M. Ezawa, O. A. Tretiakov, H. T. Diep, G. Zhao, X. Liu, and Y. Zhou: *Appl. Phys. Lett.*, **118**, 052411 (2021).
54) R. Zarzuela, D. Hill, J. Sinova, and Y. Tserkovnyak: *Phys. Rev. B*, **103**, 174424 (2021).
55) C. Psaroudaki and C. Panagopoulos: *Phys. Rev. Lett.*, **127**, 067201 (2021).
56) X. Zhang, J. Xia, O. A. Tretiakov, H. T. Diep, G. Zhao, J. Yang, Y. Zhou, M. Ezawa, and X. Liu: *Phys. Rev. B*, **104**, L220406 (2021).
57) J. Xia, X. Zhang, O. A. Tretiakov, H. T. Diep, J. Yang, G. Zhao, M. Ezawa, Y. Zhou, and X. Liu: *Phys. Rev. B*, **105**, 214402 (2022).
58) M. Miyata, J.-i. Ohe, and G. Tatara: *Phys. Rev. Applied*, **18**, 014075 (2022).
59) I. F. Sharafullin, M. K. Kharrasov, and H. T. Diep: *Phys. Rev. B*, **99**, 214420 (2019).
60) J. Xia, X. Zhang, X. Liu, Y. Zhou, and M. Ezawa: *arXiv preprint arXiv:2204.04589*, (2022).
61) X. Yu: *J. Magn. Magn. Mater.*, **539**, 168332 (2021).
62) S. Rohart and A. Thiaville: *Phys. Rev. B*, **88**, 184422 (2013).
63) C. Reichhardt, D. Ray, and C. J. O. Reichhardt: *New J. Phys.*, **17**, 073034 (2015).
64) C. Reichhardt and C. J. O. Reichhardt: *Phys. Rev. B*, **94**, 094413 (2016).
65) J. Müller: *New J. Phys.*, **19**, 025002 (2017).
66) I. Lima Fernandes, J. Bouaziz, S. Blügel, and S. Lounis: *Nat. Commun.*, **9**, 4395 (2018).
67) L. González-Gómez, J. Castell-Queralt, N. Del-Valle, A. Sanchez, and C. Navau: *Phys. Rev. B*, **100**, 054440 (2019).
68) J. Castell-Queralt, L. González-Gómez, N. Del-Valle, A. Sanchez, and C. Navau: *Nanoscale*, **11**, 12589 (2019).
69) S. Bhatti and S. N. Piramanayagam: *Phys. Status Solidi RRL*, **13**, 1900090 (2019).
70) X. Zhang, J. Xia, K. Shirai, H. Fujiwara, O. A. Tretiakov, M. Ezawa, Y. Zhou, and X. Liu: *Commun. Phys.*, **4**, 255 (2021).
71) J. C. B. Souza, N. P. Vizarim, C. J. O. Reichhardt, C. Reichhardt, and P. A. Venegas: *Phys. Rev. B*, **104**, 054434 (2021).
72) J. Souza, N. Vizarim, C. Reichhardt, C. Reichhardt, and P. Venegas: *arXiv preprint arXiv:2204.11906*, (2022).
73) X. Zhang, J. Xia, and X. Liu: *Phys. Rev. B*, **106**, 094418 (2022).
74) N. Del-Valle, J. Castell-Queralt, L. González-Gómez, and C. Navau: *APL Mater.*, **10**, 010702 (2022).
75) K. Ohara, X. Zhang, Y. Chen, Z. Wei, Y. Ma, J. Xia, Y. Zhou, and X. Liu: *Nano Lett.*, **21**, 4320 (2021).
76) R. Juge, K. Bairagi, K. G. Rana, J. Vogel, M. Sall, D. Mailly, V. T. Pham, Q. Zhang, N. Sisodia, M. Foerster, L. Aballe, M. Belmeguenai, Y. Roussigné, S. Auffret, L. D. Buda-Prejbeanu, G. Gaudin, D. Ravelosona, and O. Boulle: *Nano Lett.*, **21**, 2989 (2021).
77) Y.-K. Park, J.-S. Kim, Y.-S. Nam, S. Jeon, J.-H. Park, K.-W. Kim, H.-W. Lee, B.-C. Min, and S.-B. Choe: *NPG Asia Mater.*, **12**, 38 (2020).
78) W. Jiang, P. Upadhyaya, W. Zhang, G. Yu, M. B. Jungfleisch, F. Y. Fradin, J. E. Pearson, Y. Tserkovnyak, K. L. Wang, O. Heinonen, S. G. E. te Velthuis, and A. Hoffmann: *Science*, **349**, 283 (2015).
79) J. Sampaio, V. Cros, S. Rohart, A. Thiaville, and A. Fert: *Nat. Nanotechnol.*, **8**, 839 (2013).
80) R. Tomasello, E. Martinez, R. Zivieri, L. Torres, M. Carpentieri, and G. Finocchio: *Sci. Rep.*, **4**, 6784 (2014).
81) X. Zhang, J. Xia, Y. Zhou, D. Wang, X. Liu, W. Zhao, and M. Ezawa: *Phys. Rev. B*, **94**, 094420 (2016).
82) M. J. Donahue and D. G. Porter, *OOMMF User's Guide, Version 1.0, Interagency Report NO. NISTIR 6376, National Institute of Standards and Technology, Gaithersburg, MD (1999)* http://math.nist.gov/oommf.

Received Oct. 05, 2022; Revised Oct. 31, 2022; Accepted Nov. 10, 2022

Editorial Committee Members・Paper Committee Members

Notice for Photocopying

編集委員・論文委員

複写をされる方へ

Journal of the Magnetics Society of Japan

Vol. 47 No. 1 (通巻第325号) 2023年1月1日発行

Vol. 47 No. 1 Published Jan. 1, 2023
by the Magnetics Society of Japan
Tokyo YWCA building Rm207, 1–8–11 Kanda surugadai, Chiyoda-ku, Tokyo 101–0062
Tel.　+81–3–5281–0106　　Fax. +81–3–5281–0107

Printed by JP Corporation Co., Ltd.
Sports Plaza building 401, 2–4–3, Shinkamata Ota-ku, Tokyo 144–0054
Advertising agency: Kagaku Gijutsu-sha

発行：(公社)日本磁気学会　101–0062　東京都千代田区神田駿河台 1–8–11　東京YWCA会館 207 号室
製作：ジェイピーシー　144–0054　東京都大田区新蒲田 2–4–3　スポーツプラザビル401　Tel.（03）6715–7915
広告取扱い：科学技術社　111–0052　東京都台東区柳橋 2–10–8　武田ビル4F　Tel.（03）5809–1132